# Highly Selective $CO_2$ Removal for One-Step Liquefied Natural Gas Processing by Physisorbents

David G. Madden,[1] Daniel O'Nolan,[1] Kai-Jie Chen,[1] Carol Hua,[1] Amrit Kumar,[1] Tony Pham,[2] Katherine A. Forrest,[2] Brian Space,[2] John J. Perry IV,[1] Majeda Khraisheh,[3] Michael J. Zaworotko[1]*

Correspondence to: xtal@ul.ie

## Materials and Methods

TIFSIX-3-Ni (*1*), NbOFFIVE-1-Ni (*2*), SIFSIX-3-Ni (*3*), TIFSIX-2-Cu-i (*4*) and Mg-MOF-74 (*5*) were synthesised according to literature procedures. Zeolite 13X was obtained from Sigma-Aldrich.

**Preparation of $\{[Ni(pyr)_2(TiF_6)]_n\}$ (TIFSIX-3-Ni) *via* slurrying method.**
Nickel hexafluorotitanate (0.500 g, 2.27 mmol) and pyrazine (2.50 g, 31.2 mmol) were dissolved in 1 mL of deionized water and stirred for 48 h at room temperature to yield a polycrystalline precursor of TIFSIX-3-Ni (blue color powder) (*1*). The precursor was air dried and heated at 160 °C for 24 h to obtain the desired TIFSIX-3-Ni. Activation of TIFSIX-3-Ni was achieved by degassing the sample on a SmartVacPrep™ using dynamic vacuum and heating for 24 h (sample heated from RT to 160 °C with a ramp rate of 10 °C/min).

**Preparation of $\{[Ni(pyr)_2(TiF_6)]_n\}$ (TIFSIX-3-Ni) *via* mechanochemical ball milling.**
Mechanochemical synthesis of TIFSIX-3-Ni was carried out by placing a mixture of nickel hexafluorotitanate (3.280 g; 10 mmol) and pyrazine (1.6 g; 20 mmol) into a 35 mL Teflon jar with two 15 mm teflon steel core grinding balls. This mixture was then ground for 180 min in a Retsch MM400 mill at 25 Hz resulting in the polycrystalline precursor of TIFSIX-3-Ni. The precursor was heated at 160 °C for 24 h to obtain the desired TIFSIX-3-Ni. Activation of TIFSIX-3-Ni was achieved by degassing the sample on a SmartVacPrep™ using dynamic vacuum and heating for 24 h (sample heated from RT to 160 °C with a ramp rate of 10 °C/min).

**Preparation of $\{[Ni(pyr)_2(NbOF_5)]_n\}$ (NbOFFIVE-1-Ni).**
The compound NbOFFIVE-1-Ni was synthesized and activated using a reported synthesis method (*2*). Nickel nitrate hexahydrate (0.175 g, 0.602 mmol), niobium (V) oxide (0.0790 g, 0.297 mmol), pyrazine (0.384 g, 4.79 mmol) and hydrofluoric acid (0.26 mL, aqueous 48%, 7.17 mmol) were added to 3 mL of deionized water in a Teflon bomb and heated at 130 °C for 24 h. Violet colored crystals were obtained upon cooling the reaction mixture to room temperature. The crystals obtained were washed with methanol to remove any traces of unreacted hydrofluoric acid. Activation of NbOFFIVE-1-Ni was carried out by degassing the methanol-washed sample on a SmartVacPrep™ using dynamic vacuum and heating for 24 h (sample heated from RT to 105 °C with a ramp rate of 10 °C/min).

**Preparation of $\{[Ni(pyr)_2(SiF_6)]\}_n$ (SIFSIX-3-Ni).**
SIFSIX-3-Ni was synthesized by slurring 870 mg (3 mmol) of $Ni(NO_3)_2$, 534 mg (3 mmol) of $(NH_4)_2SiF_6$ and 480 mg (6 mmol) of pyrazine in 4 ml of water for 2 days (*6*). The produced

suspension was filtered under vacuum and dried on air. This precursor was soaked in methanol for 1 day and then washed twice with two small portions (ca. 10 ml) of methanol on a Buchner filter. After being dried in air, it was heated at 140 ˚C for 1 day to obtain SIFSIX-3-Ni. Activation of SIFSIX-3-Ni was achieved by degassing the methanol-exchanged sample on a SmartVacPrep™ using dynamic vacuum and heating for 24 hours (sample heated from RT to 140 ˚C with a ramp rate of 10 ˚C).

**Preparation of $\{[Cu(dpa)_2(TiF_6)]\}_n$ (TIFSIX-2-Cu-i).**
$Cu(NO_3)_2 \cdot 3H_2O$ (100 mg, 0.416 mmol) and $(NH_4)_2TiF_6$ (82 mg, 0.416 mmol) were dissolved in 5 ml of $H_2O$ and the solution stirred (*4*). Separately, 1,2-bis(4-pyridyl)acetylene (2) (150 mg, 0.833mmol) was dissolved in 15 ml MeCN and added dropwise to the stirring aqueous solution. A pale blue precipitate appeared immediately and the solution was left stirring for 24 hours. After this time the solution was left to sit and the solvent decanted and replaced with 10 ml fresh MeCN twice a day for one week. Following this, the solution was filtered and the precipitate washed with MeCN and dried in air. TIFSIX-2-Cu-i samples were dried in the air and degassed under high vacuum at room temperature for 16 hours before used for sorption experiments.

**Preparation of $Mg_2(dobdc)$ (Mg-MOF-74, CPO-27-Mg; dobdc = 2,5-dioxido-1,4-benzenedicarboxylate).**
The compound $Mg_2(dobdc)$ was synthesized and activated using a modified synthesis from previous reports (*7*). $H_4dobdc$ (1.11 g, 5.6 mmol) and $Mg(NO_3)_2 \cdot 6H_2O$ (4.75 g, 18.6 mmol) were dissolved in a 15:1:1 (v/v/v) mixture of DMF:ethanol:$H_2O$ (500 mL) and sparged using $N_2$ for 1 h. The resulting solution was distributed into thirty-five 20 mL vials, which were sealed with Teflon-lined caps and heated to 120 °C for 8 h. Following the reaction, the resulting yellow material was washed repeatedly with DMF. The DMF was decanted and replaced with fresh DMF repeatedly for a week, refreshing the DMF twice daily. Then, the DMF was decanted and replaced by methanol (MeOH). The MeOH was decanted, and replaced with fresh MeOH twice daily for a further three days. The resulting dark yellow powder was collected by filtration and then activated under vacuum at 180 °C for 24-48 h.

**Preparation of Zeolite 13X (Na-X, FAU; $Na_{50}Al_{50}Si_{59}O_{218}$).**
Zeolite 13X was purchased as a pure powder from Sigma-Aldrich. The zeolite was activated by heating at 250 °C under vacuum for 24 h as per previous reports (*7*).

**Powder X-ray Diffraction (PXRD).**
Diffractograms were recorded using a PANalytical Empyrean™ diffractometer equipped with a PIXcel$^{3D}$ detector operating in scanning line detector mode with an active length of 4 utilizing 255 channels. The diffractometer is outfitted with an Empyrean Cu LFF (long fine-focus) HR (9430 033 7310x) tube operated at 40 kV and 40 mA and CuKα radiation (λα = 1.540598 Å) was used for diffraction experiments. Continuous scanning mode with the goniometer in the theta-theta orientation was used to collect the data. Incident beam optics included the Fixed Divergences slit with anti-scatter slit PreFIX module, with a 1/8° divergence slit and a 1/4° anti-scatter slit, as well as a 10 mm fixed incident beam mask and a Soller slit (0.04 rad). Divergent beam optics included a P7.5 anti-scatter slit, a Soller slit (0.04 rad), and a Ni-β filter. In a typical experiment, 20 mg of sample was dried, ground into a fine powder and was loaded on a zero background silicon disks. The data was collected from 5°-45° (2θ) with a step-size of 0.02626° and a scan time of 29 seconds per step. Crude data was analyzed using the X'Pert HighScore Plus™ software V 4.1 (PANalytical, The Netherlands). Plots of stacked PXRD spectra for each adsorbent displaying the diffraction pattern for calculated and as synthesized materials are provided below (Fig. S1-S6).

**Gas Sorption Measurements.**
Ultra-high-purity grade $N_2$, $CH_4$ and $CO_2$ were used for gas sorption experiments. Adsorption experiments (up to 1 bar) for different pure gases were performed on Micromeritics TriStar II PLUS and Micromeritics 3 Flex surface area and pore size analyzer. Measurements with $N_2$ at 77 K were conducted on a Micromeritics TriStar II PLUS instrument. Brunauer-Emmett-Teller (BET) surface areas were determined from the $N_2$ adsorption isotherms at 77 K using the Micromeritics Microactive software except for NbOFFIVE-1-Ni, SIFSIX-3-Ni and TIFSIX-3-Ni whose BET surface areas were determined from the $CO_2$ adsorption isotherms collected at 298 K. About 200 mg of activated samples were used for the measurements. Very low-pressure $CO_2$ measurements were performed on a Micromeritics 3 Flex surface area and pore size analyser at 273, 283, 293 and 298 K. A Julabo temperature controller was used to maintain a constant temperature in the bath through the duration of the experiment. Samples were degassed on a Smart VacPrep instrument prior to the analysis.

**Dynamic Gas Breakthrough Measurement Studies.**
In a typical experiment, *ca.* 0.3 g of finely ground pre-activated sample was placed in a quartz tube (Ø = 8 mm) to form a fixed bed held in place using quartz wool. Each sample was heated to 353 K under a dry helium flow to remove atmospheric contaminants. Upon cooling, a $CO_2/CH_4$ mixture (1/99 and 50/50 *v/v*) was passed over the packed bed with a total flow rate of 10 $cm^3$/min at 298 K. The outlet gas concentration was continuously monitored using an Hiden HPR-20 QIC evolved gas analysis mass spectrometer (EGA-MS). Upon complete breakthrough and saturation of the packed bed adsorbent, the gas mixed is switched off and dry helium was flowed over the solid. Heating was switch on and samples were heated to 353 K to aid regeneration.

**Calculation of IAST Selectivities**
The $CO_2/CH_4$ selectivities for the adsorbate mixture composition of interest (1/99 and 50/50) in TIFSIX-3-Ni, SIFSIX-3-Ni, NbOFFIVE-1-Ni, TIFSIX-2-Cu-i, Mg-MOF-74 and Zeolite 13X were predicted from the single-component adsorption isotherms using Ideal Adsorbed Solution Theory (IAST) (*8*), as employed in IAST++. First, the single-component isotherms for the adsorbates at 298 K were fitted to the dual-site Langmuir-Freundlich equation (Table S1-S6):

$$n(P) = \frac{n_{m1} b_1 P^{\left(\frac{1}{t_1}\right)}}{1 + b_1 P^{\left(\frac{1}{t_1}\right)}} + \frac{n_{m2} b_2 P^{\left(\frac{1}{t_2}\right)}}{1 + b_2 P^{\left(\frac{1}{t_2}\right)}}$$

In this equation, $n$ is the amount adsorbed per mass of material (in mmol $g^{-1}$), $P$ is the total pressure (in kPa) of the bulk gas at equilibrium with the adsorbed phase, $n_{m1}$ and $n_{m2}$ are the saturation uptakes (in in mmol $g^{-1}$) for sites 1 and 2, $b_1$ and $b_2$ are the affinity coefficients (in $kPa^{-1}$) for sites 1 and 2, and $t_1$ and $t_2$ represent the deviations from the ideal homogeneous surface (unitless) for sites 1 and 2. The parameters that were obtained from the fitting for TIFSIX-3-Ni, SIFSIX-3-Ni, NbOFFIVE-1-Ni, TIFSIX-2-Cu-i, Mg-MOF-74 and Zeolite 13X are found in Tables S1-S6, respectively. All isotherms were fitted with $R^2 > 0.999$. Next, the spreading pressure for adsorbates *i* and *j* can be calculated using the following equations:

$$\frac{\pi^{\circ}_{i}A}{RT} = \int_{0}^{P^{\circ}_{i}(\pi)} \frac{n_i(P)}{P} dP$$

$$\frac{\pi^{\circ}_{j}A}{RT} = \int_{0}^{P^{\circ}_{j}(\pi)} \frac{n_j(P)}{P} dP$$

In the above equations, $A$ represents the specific surface area (assumed to be the same for all adsorbates), $R$ is the ideal gas constant, $T$ is the temperature, and $P°_i(\pi)$ and $P°_j(\pi)$ are the equilibrium gas phase pressures corresponding to the solution temperature and solution spreading pressure for the adsorption of pure components $i$ and $j$, respectively. Further, the following equations hold true for a two-component mixture according to IAST:

$$\pi^{\circ}_{i} = \pi^{\circ}_{j}$$

$$Py_i = P^{\circ}_{i}x_i$$

$$Py_i = P^{\circ}_{i}x_i$$

$$x_i + x_j = 1$$

$$y_i + y_j = 1$$

Here, $x_i$ and $x_j$ are the mole fractions of components $i$ and $j$, respectively, in the adsorbed phase, and $y_i$ and $y_j$ are the mole fractions of components $i$ and $j$, respectively, in the gas phase. The previous seven equations are seven independent equations with nine unknowns. In order to solve for all of the unknowns, two quantities must be specified, particularly $P$ and $y_i$. Utilization of the aforementioned equations yields the following equilibrium expression for adsorbates $i$ and $j$:

$$\int_{0}^{\frac{Py_i}{x_i}} \frac{n_i(P)}{P} dP = \int_{0}^{\frac{P(1-y_i)}{(1-x_i)}} \frac{n_j(P)}{P} dP$$

The above equation was solved for $x_i$ using numerical analysis[3] for a range of pressures at a specified $y_i$ value. Finally, the selectivity for adsorbate $i$ relative to adsorbate $j$ was calculated using the following:

$$S_{i/j} = \frac{x_i y_j}{x_j y_i}$$

**Modeling Studies**

Periodic density functional theory (DFT) were performed to evaluate the binding site and adsorption energy ($\Delta E$) for $CH_4$ in TIFSIX-2-Cu-i, SIFSIX-3-Ni, and TIFSIX-3-Ni. These calculations were implemented with the Vienna *ab initio* Simulation Package (VASP)(*9-12*) with the projector augmented wave (PAW) method (*13, 14*) with the Perdew–Burke–Ernzerhof (PBE) functional (*15, 16*). Furthermore, dispersion effects were treated using the DFT-D2 correction method of Grimme (*17*).

The position of a single $CH_4$ molecule was initially optimized within the rigid unit cell of the respective HUMs. Afterward, another optimization was carried out in which the position of all atoms and lattice parameters of the system were allowed to vary. The optimized position of a $CH_4$ molecule within TIFSIX-2-Cu-i, SIFSIX-3-Ni, and TIFSIX-3-Ni are displayed in Figures S20, S21, and S22, respectively. The $\Delta E$ for $CH_4$ in all three HUMs was calculated by the following:

$$\Delta E = E(\text{HUM} + \text{CH}_4) - E(\text{HUM}) - E(\text{CH}_4)$$

Where $E(\text{HUM} + \text{CH}_4)$ is the energy of the unit cell of the HUM with $CH_4$, $E(\text{HUM})$ is the energy of the empty unit cell, and $E(\text{CH}_4)$ is the energy of the $CH_4$. The calculated $\Delta E$ values for $CH_4$ in TIFSIX-2-Cu-i, SIFSIX-3-Ni, and TIFSIX-3-Ni are displayed in Table S7.

**Isosteric Heats of Adsorption Calculations**

The $Q_{st}$ of $CO_2$ for TIFSIX-3-Ni, NbOFFIVE-1-Ni, SIFSIX-3-Ni, TIFSIX-2-Cu-i, Mg-MOF-74, and Zeolite 13X were calculated from the low-pressure $CO_2$ adsorption isotherms collected at 273, 283 and 293 K. The Clausius-Clapeyron equation was used for the calculation of $Q_{st}$ where virial-type equations were used to fit ten points in the adsorption data between 0 and 3000 ppm at multiple temperatures.

$$\ln P = \ln n + (\frac{1}{T^2}) \sum_{i=0}^{j} a_i n^i + \sum_{i=0}^{k} b_i n^i$$

The $Q_{st}$ was then calculated from the virial model.

$$-Q_{st} = -R \sum_{i=0}^{j} a_i n^i$$

Ten adsorption points between 0 and 3000 ppm (0.3 mbar) were used for fitting to the Virial equation where the fit for each of the compounds is shown below.

**Supplementary Table 1: Dual-site Langmuir-Freundlich fitting paprameters.**
The fitted parameters for the dual-site Langmuir-Freundlich equation for the single-component isotherms of $CO_2$ and $CH_4$ in TIFSIX-3-Ni at 298 K. The $R^2$ value is also provided.

| **TIFSIX-3-Ni** | **$CO_2$** | **$CH_4$** |
|---|---|---|
| **q1** | 1.62E-16 | 2.93139 |
| **n2** | 0.930398 | 0.805388 |
| **k1** | 3.69E-11 | 0.127172 |
| **k2** | 2361.64 | 0.685037 |
| **n1** | 1.15E-06 | 1.46179 |
| **q2** | 2.19488 | 0.147156 |
| **R^2** | 0.999908 | 0.999876 |

**Supplementary Table 2: Dual-site Langmuir-Freundlich fitting parameters.**
The fitted parameters for the dual-site Langmuir-Freundlich equation for the single-component isotherms of $CO_2$ and $CH_4$ in NbOFFIVE-1-Ni at 298 K. The $R^2$ value is also provided.

| **NbOFFIVE-1-Ni** | **$CO_2$** | **$CH_4$** |
|---|---|---|
| **q1** | 0.25617 | 0.296557 |
| **n2** | 0.99632 | 0.693746 |
| **k1** | 2.62E-10 | 0.507841 |
| **k2** | 2638.04 | 0.096855 |
| **n1** | 0.00827069 | 2.50422 |
| **q2** | 2.18654 | 0.324598 |
| **R^2** | 0.999998 | 0.997273 |

**Supplementary Table 3: Dual-site Langmuir-Freundlich fitting parameters.**
The fitted parameters for the dual-site Langmuir-Freundlich equation for the single-component isotherms of $CO_2$ and $CH_4$ in SIFSIX-3-Ni at 298 K. The $R^2$ value is also provided.

| **SIFSIX-3-Ni** | **$CO_2$** | **$CH_4$** |
|---|---|---|
| **q1** | 2.35E-16 | 5.36E-05 |
| **n2** | 0.88157 | 1.04056 |
| **k1** | 1.12567 | 3034.22 |
| **k2** | 237.238 | 0.121931 |
| **n1** | 5.96E-08 | 87.3381 |
| **q2** | 2.63469 | 2.91988 |
| **R^2** | 0.999703 | 0.999999 |

**Supplementary Table 4: Dual-site Langmuir-Freundlich fitting parameters.**

The fitted parameters for the dual-site Langmuir-Freundlich equation for the single-component isotherms of $CO_2$ and $CH_4$ in TIFSIX-2-Cu-i at 298 K. The $R^2$ value is also provided.

| **TIFSIX-2-Cu-i** | **$CO_2$** | **$CH_4$** |
|---|---|---|
| **q1** | 697.127 | 1.19963 |
| **n2** | 0.995968 | 1.46461 |
| **k1** | 0.000382108 | 0.208933 |
| **k2** | 5.10501 | 0.225437 |
| **n1** | 0.935309 | 0.800206 |
| **q2** | 4.58447 | 4.76338 |
| **R^2** | 0.999997 | 0.999984 |

**Supplementary Table 5: Dual-site Langmuir-Freundlich fitting parameters.**

The fitted parameters for the dual-site Langmuir-Freundlich equation for the single-component isotherms of $CO_2$ and $CH_4$ in Mg-MOF-74 at 298 K. The $R^2$ value is also provided.

| **Mg-MOF-74** | **$CO_2$** | **$CH_4$** |
|---|---|---|
| **q1** | 8.36122 | 0.123771 |
| **n2** | 0.982777 | 1.01852 |
| **k1** | 0.391968 | 1.0456 |
| **k2** | 40.6107 | 0.243348 |
| **n1** | 0.988838 | 5.24771 |
| **q2** | 4.75802 | 4.82979 |
| **R^2** | 0.999999 | 0.999984 |

**Supplementary Table 6: Dual-site Langmuir-Freundlich fitting parameters.**

The fitted parameters for the dual-site Langmuir-Freundlich equation for the single-component isotherms of $CO_2$ and $CH_4$ in Zeolite 13X at 298 K. The $R^2$ value is also provided.

| **Zeolite 13X** | **$CO_2$** | **$CH_4$** |
|---|---|---|
| **q1** | 3.34E-15 | 1.69432 |
| **n2** | 0.528859 | 0.996942 |
| **k1** | 5.39E-08 | 0.449284 |
| **k2** | 22.0372 | 1.01729 |
| **n1** | 0.145623 | 1.71694 |
| **q2** | 7.11861 | 0.755876 |
| **R^2** | 0.999643 | 0.999998 |

**Supplementary Table 7: Single point sorption energy.**

Calculated adsorption energies (in kJ $mol^{-1}$) for a single $CH_4$ molecule within the unit cell of TIFSIX-2-Cu-i, SIFSIX-3-Ni, and TIFSIX-3-Ni as determined from periodic DFT calculations using VASP.

| **HUM** | **$\Delta E$ (kJ $mol^{-1}$)** |
|---|---|
| **TIFSIX-2-Cu-i** | –24.41 |
| **SIFSIX-3-Ni** | –30.24 |
| **TIFSIX-3-Ni** | –30.26 |

**Supplementary Table 8: Virial equation fitting parameters.**

Fitting parameters for TIFSIX-3-Ni.

| **Parameters** | **Value** | **Standard Error** |
|---|---|---|
| **a0** | -5643.77909 | 233.09913 |
| **a1** | -3582.12507 | 699.32213 |
| **a2** | 4493.99446 | 749.85233 |
| **a3** | -2281.59589 | 340.83247 |
| **a4** | 436.56659 | 55.92704 |
| **a5** | 0 | 0 |
| **b0** | 25.43248 | 0.18808 |
| **b1** | 0 | 0 |
| **b2** | 0 | 0 |
| **b3** | 0 | 0 |
| **Reduced Chi-Sqr** | 3.15597E-4 | |
| **Adj. R-Square** | 0.9996 | |

**Supplementary Table 9: Virial equation fitting parameters.**

Fitting parameters for NbOFFIVE-1-Ni.

| **Parameters** | **Value** | **Standard Error** |
|---|---|---|
| **a0*** | -6505.48297 | 26.67 |
| **a1*** | 7835.26561 | 190.22955 |
| **a2*** | -5431.6051 | 390.59188 |
| **a3*** | -5287.61987 | 670.44476 |
| **a4*** | 2886.31126 | 501.75741 |
| **a5*** | 0 | 0 |
| **b0*** | 25.53873 | 0.09338 |
| **b1*** | -30.99931 | 0.65225 |
| **b2*** | 31.51595 | 0.96432 |
| **b3*** | 0 | 0 |
| **Reduced Chi-Sqr** | 4.13E-05 | |
| **Adj. R-Square** | 0.99996 | |

**Supplementary Table 10: Virial equation fitting parameters.**
Fitting parameters for SIFSIX-3-Ni.

| Parameters | Value | Standard Error |
|---|---|---|
| **a0** | -5275.96689 | 35.74562 |
| **a1** | -658.17726 | 87.8135 |
| **a2** | 639.49304 | 52.52675 |
| **a3** | -367.67605 | 26.83061 |
| **a4** | 99.0502 | 6.83313 |
| **a5** | 0 | 0 |
| **b0** | 22.41777 | 0.1273 |
| **b1** | 1.56213 | 0.31722 |
| **b2** | -0.15424 | 0.17365 |
| **b3** | 0 | 0 |
| **Reduced Chi-Sqr** | 1.94117E-5 | |
| **Adj. R-Square** | 0.99999 | |

**Supplementary Table 11: Virial equation fitting parameters.**
Fitting parameters for TIFSIX-2-Cu-i.

| Parameters | Value | Standard Error |
|---|---|---|
| **a0** | -4193.93074 | 21.75433 |
| **a1** | 88.2787 | 6.94223 |
| **a2** | -16.36871 | 2.43793 |
| **a3** | 4.59481 | 0.25199 |
| **b0** | 22.14176 | 0.07389 |
| **Adj. R-Square** | 0.99842 | |

**Supplementary Table 12: Virial equation fitting parameters.**

Fitting parameters for Mg-MOF-74.

| Parameters | Value | Standard Error |
|---|---|---|
| **a0** | -5097.16475 | 18.97529 |
| **a1** | 574.65484 | 82.27637 |
| **a2** | -321.76928 | 83.09131 |
| **a3** | 82.79407 | 17.78506 |
| **a4** | -17.52221 | 4.63194 |
| **a5** | 0 | 0 |
| **b0** | 15.93129 | 0.06358 |
| **b1** | -1.50837 | 0.26696 |
| **b2** | 0.68876 | 0.23788 |
| **b3** | 0 | 0 |
| **Reduced Chi-Sqr** | 6.37182E-6 | |
| **Adj. R-Square** | 0.99999 | |

**Supplementary Table 13: Virial equation fitting parameters.**

Fitting parameters for Zeolite 13X.

| Parameters | Value | Standard Error |
|---|---|---|
| **a0** | -4800.00613 | 132.39722 |
| **a1** | 797.61373 | 176.85271 |
| **a2** | -676.20166 | 219.18557 |
| **a3** | 433.94642 | 160.8827 |
| **a4** | -104.16306 | 40.50343 |
| **a5** | 0 | 0 |
| **b0** | 19.70324 | 0.46117 |
| **b1** | 0.19534 | 0.45833 |
| **b2** | 0 | 0 |
| **b3** | 0 | 0 |
| **Reduced Chi-Sqr** | 7.78166E-4 | |
| **Adj. R-Square** | 0.99954 | |

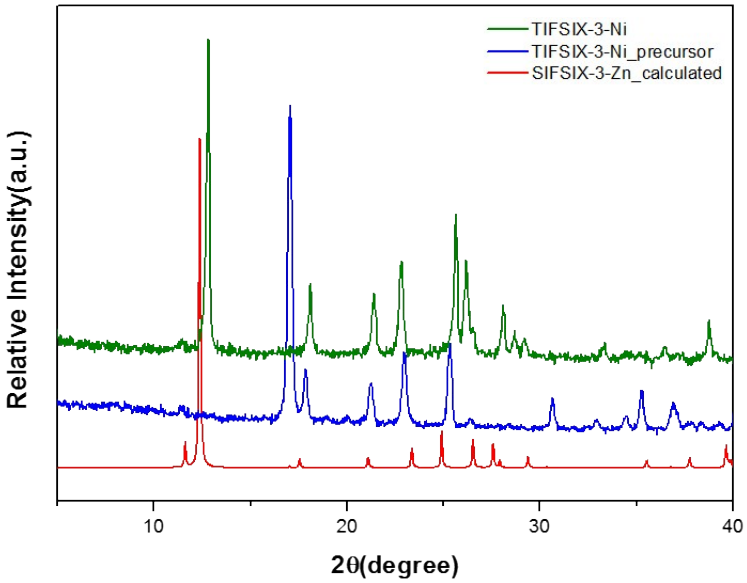


**Supplementary Figure 1.**
Powder X-ray diffraction (PXRD) of TIFSIX-3-Ni.

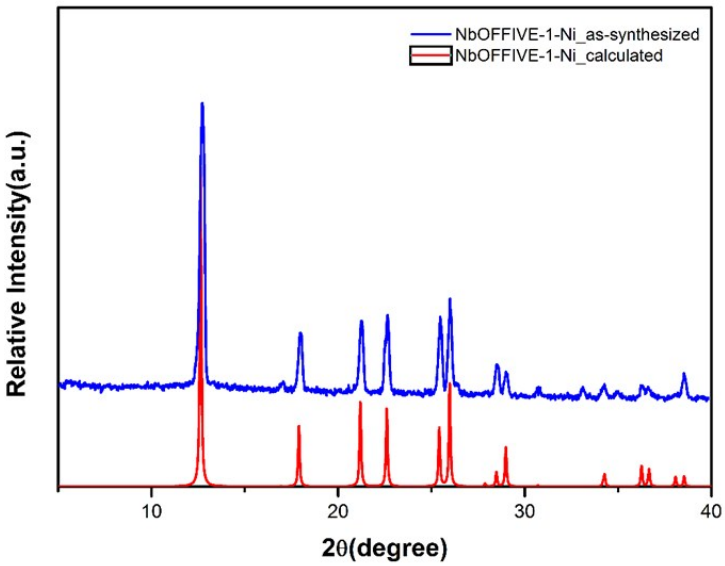


**Supplementary Figure 2.**
Powder X-ray diffraction (PXRD) of NbOFFIVE-1-Ni.

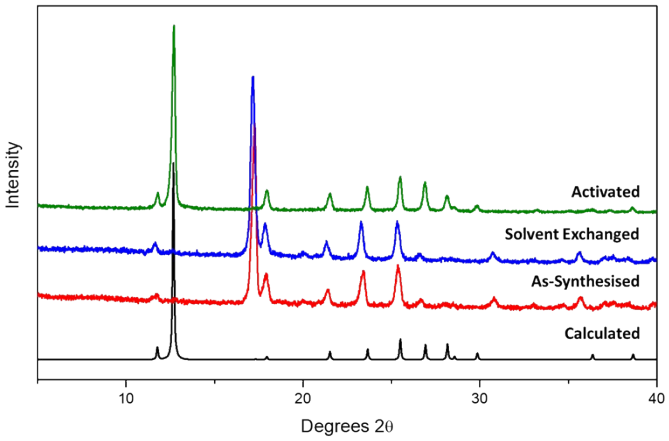


**Supplementary Figure 3.**
Powder XRDs of SIFSIX-3-Ni as synthesised and after sorption *vs*. the calculated pattern.

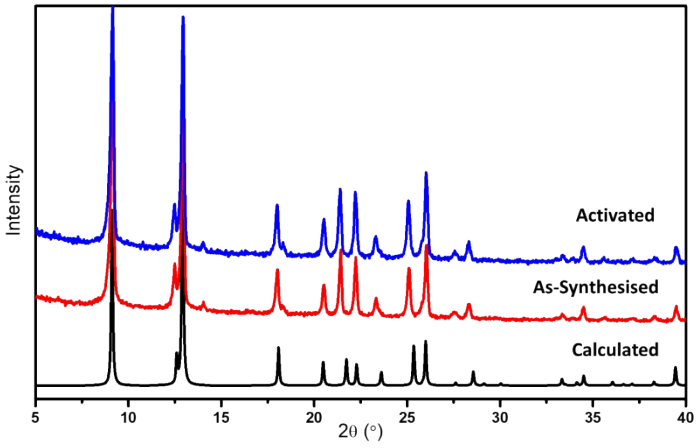


**Supplementary Figure 4.**
Powder XRDs of TIFSIX-2-Cu-i as synthesised and after sorption *vs*. the calculated pattern.

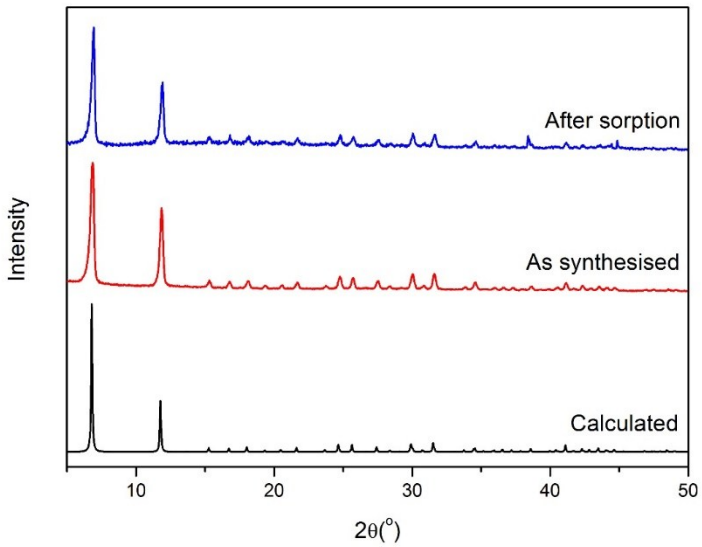


**Supplementary Figure 5.**
Powder XRDs of Mg-MOF-74 as synthesised and after sorption *vs*. the calculated pattern.

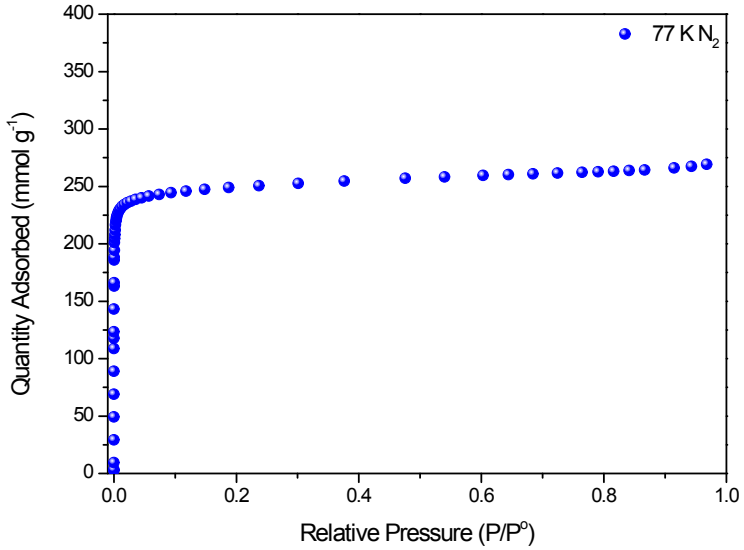


**Supplementary Figure 6.**
Sorption isotherms for 77 K $N_2$ for Mg-MOF-74.

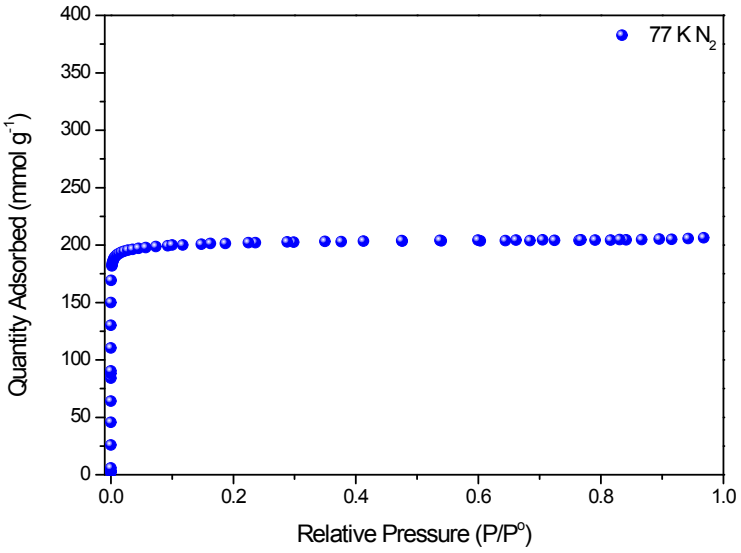


**Supplementary Figure 7.**
Sorption isotherms for 77 K $N_2$ for Zeolite 13X.

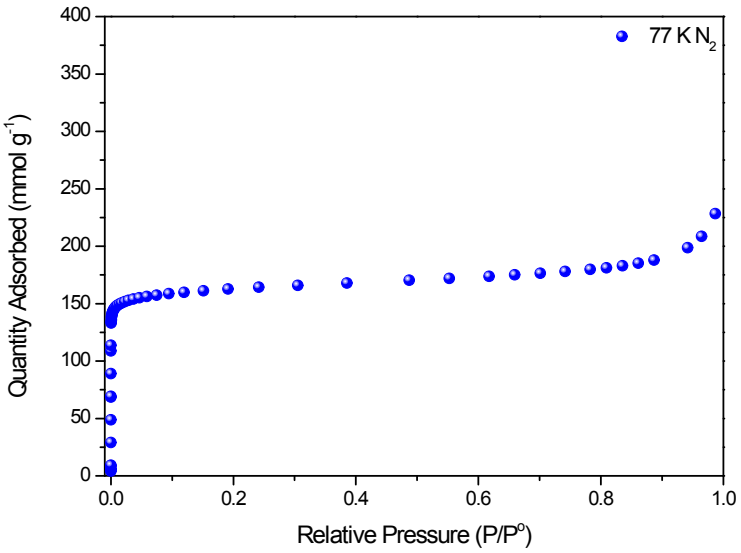


**Supplementary Figure 8.**
Sorption isotherms for 77 K $N_2$ for TIFSIX-2-Cu-i.

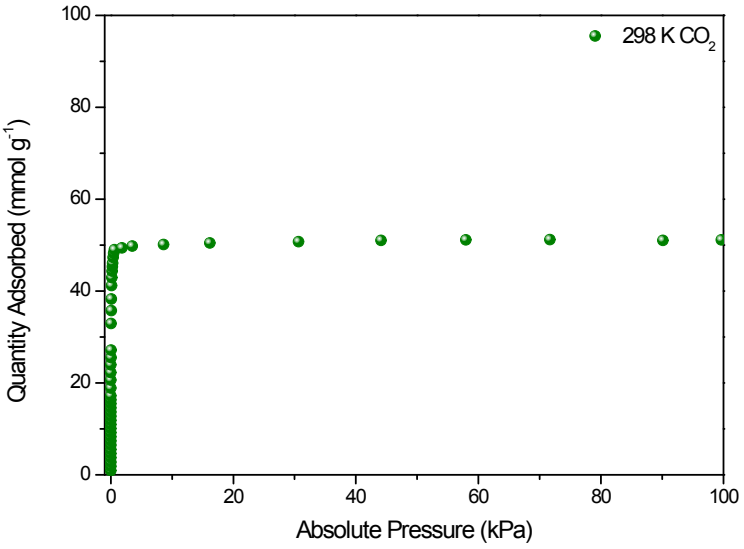


**Supplementary Figure 9.**
Sorption isotherms for 298 K $CO_2$ for NbOFFIVE-1-Ni.

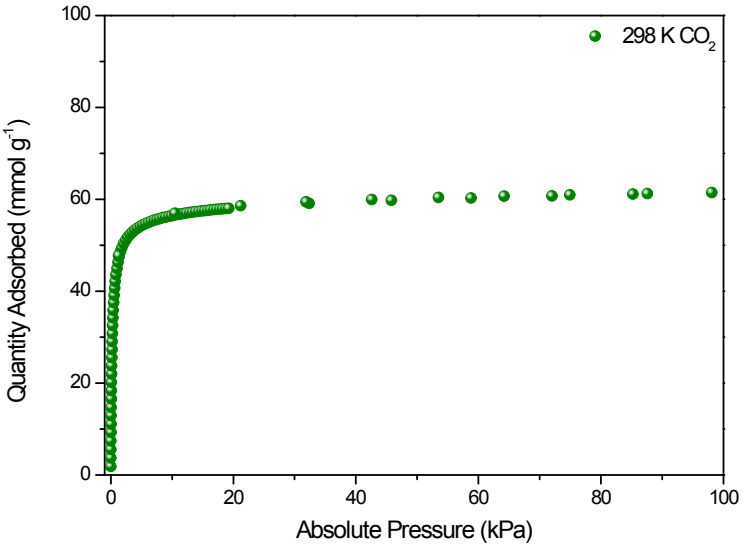


**Supplementary Figure 10.**
Sorption isotherms for 298 K $CO_2$ for SIFSIX-3-Ni.

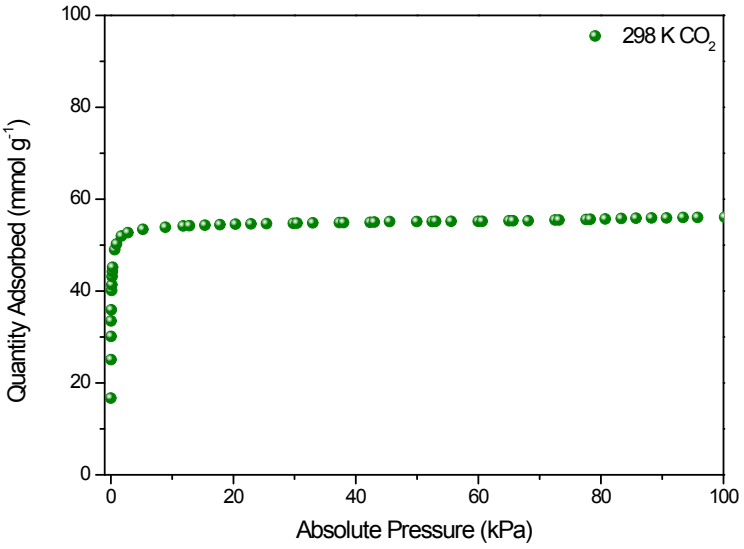


**Supplementary Figure 11.**
Sorption isotherms for 298 K $CO_2$ for TIFSIX-3-Ni.

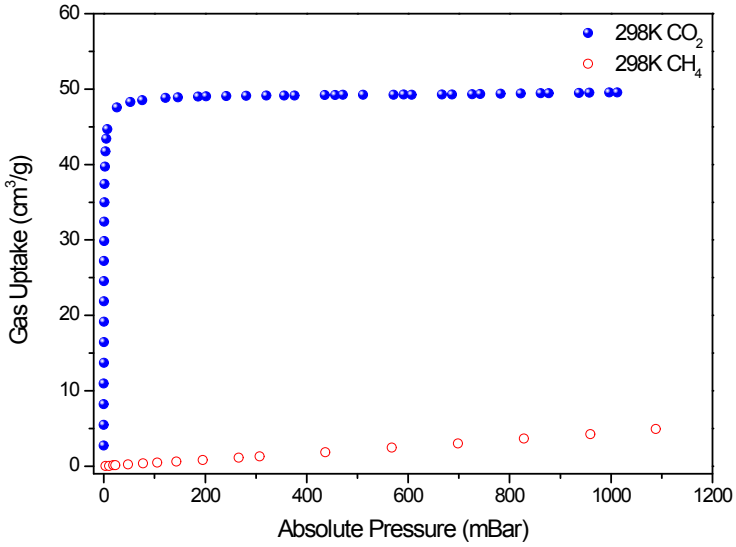


**Supplementary Figure 12.**
Sorption isotherms for $CO_2$ and $CH_4$ for TIFSIX-3-Ni at 298 K.

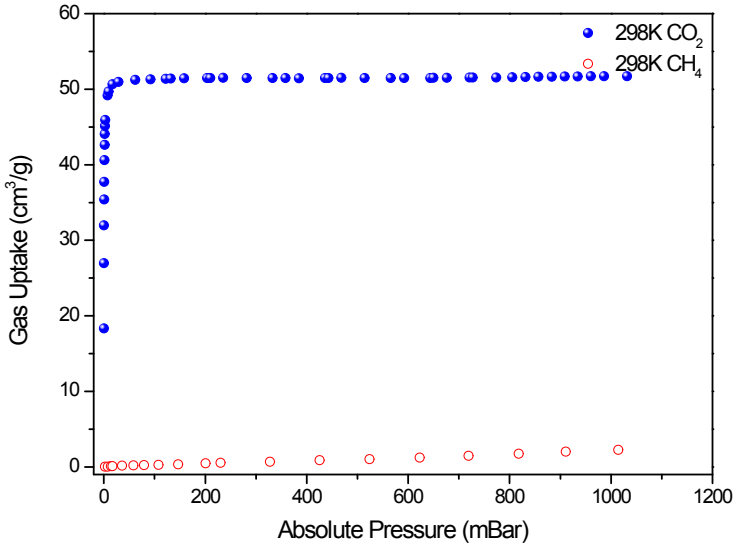


**Supplementary Figure 13.**
Sorption isotherms for $CO_2$ and $CH_4$ for NbOFFIVE-1-Ni at 298 K.

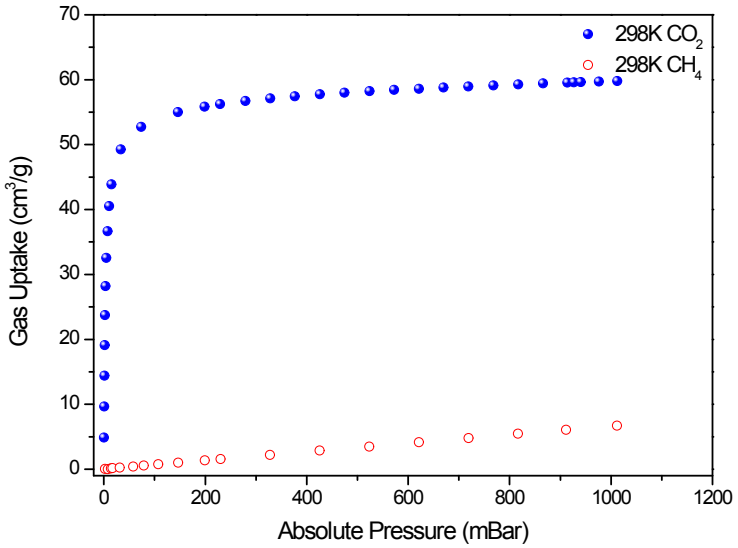


**Supplementary Figure 14.**
Sorption isotherms for $CO_2$ and $CH_4$ for SIFSIX-3-Ni at 298 K.

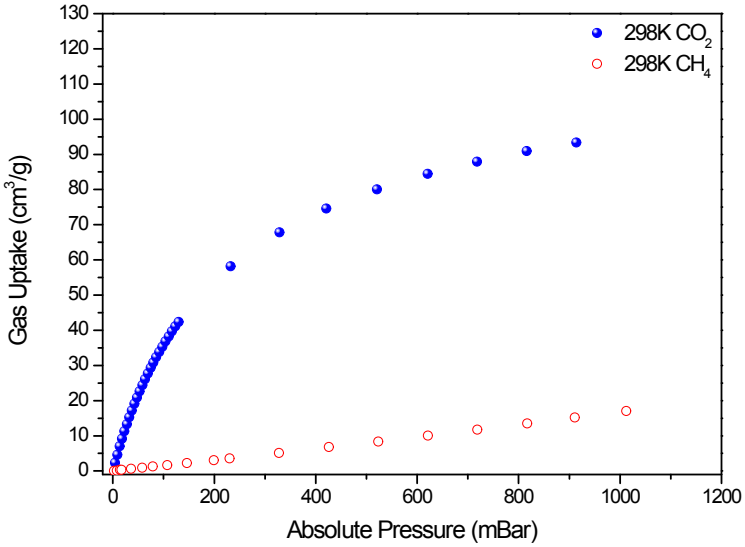


**Supplementary Figure 15.**
Sorption isotherms for $CO_2$ and $CH_4$ for TIFSIX-2-Cu-i at 298 K.

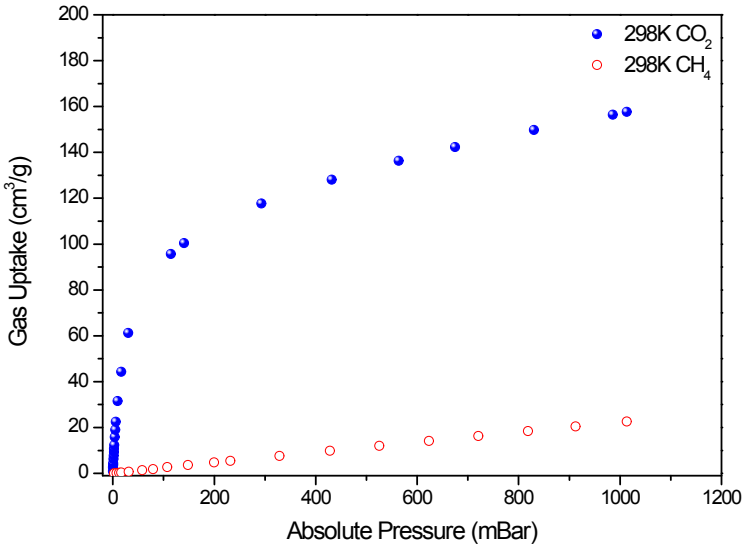


**Supplementary Figure 16.**
Sorption isotherms for $CO_2$ and $CH_4$ for Mg-MOF-74 at 298 K.

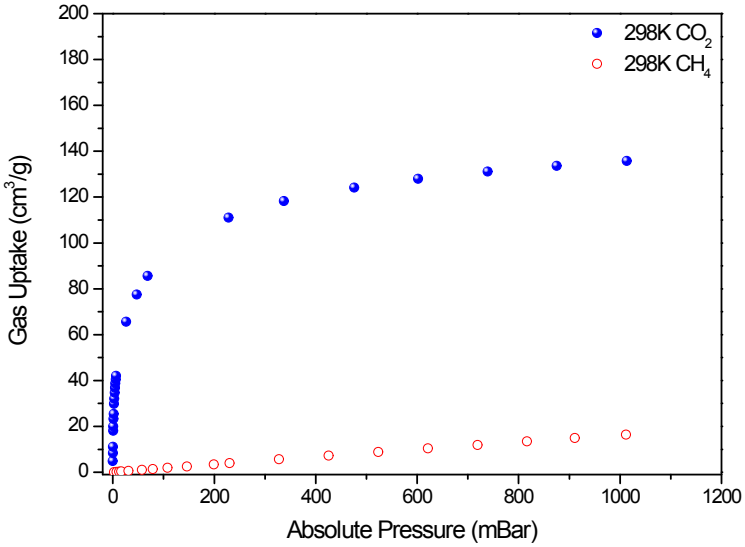


**Supplementary Figure 17.**
Sorption isotherms for $CO_2$ and $CH_4$ for Zeolite 13X at 298 K.

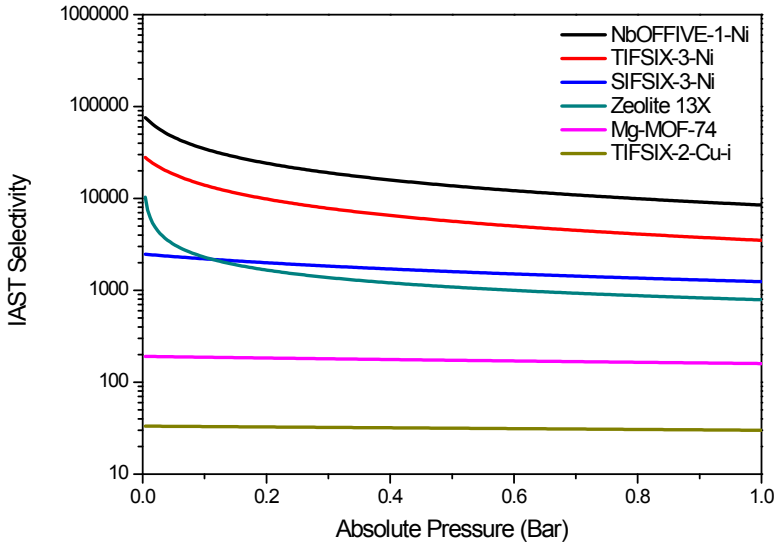


**Supplementary Figure 18.**
IAST Selectivity's for 1/99 $CO_2/CH_4$ Gas Mixtures at 298 K.

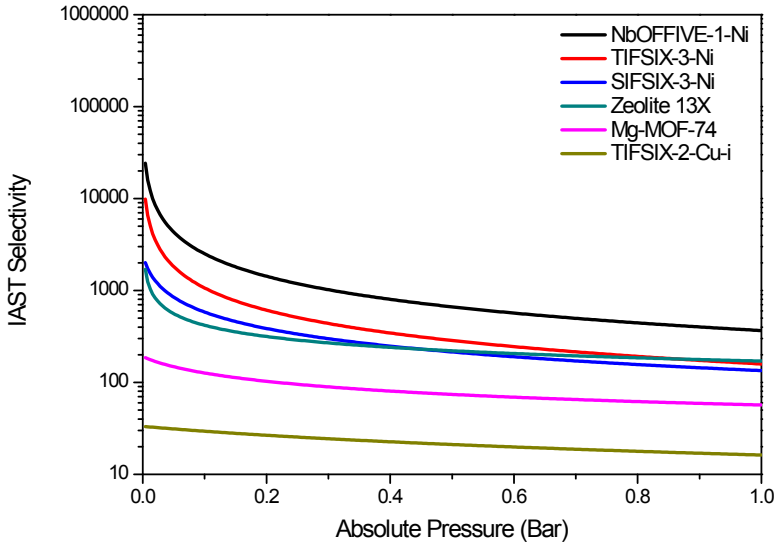


**Supplementary Figure 19.**
IAST Selectivity's for 50/50 $CO_2/CH_4$ Gas Mixtures at 298 K.

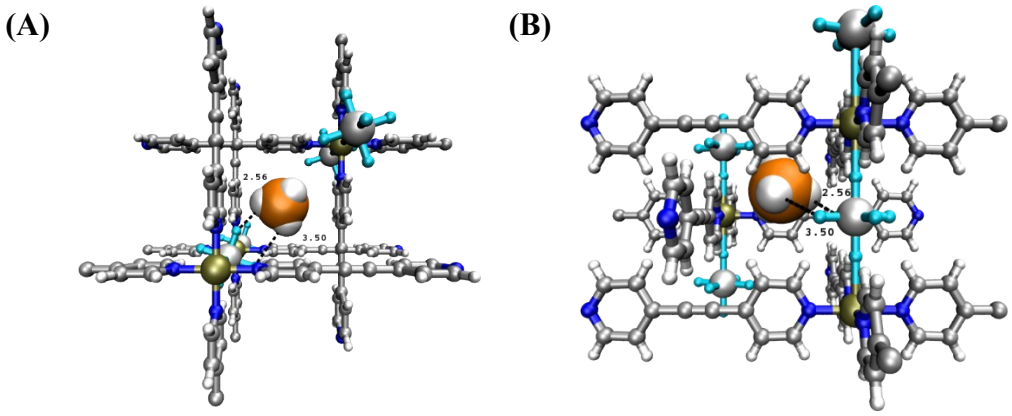


**Supplementary Figure 20.**
Molecular modelling of $CH_4$ binding site in TIFSIX-2-Cu-i. (**A**) *c*-axis view (**B**) and *a*/*b*-axis view of a portion of the crystal structure of TIFSIX-2-Cu-i showing the optimized position of a $CH_4$ molecule in the HUM as determine through periodic DFT calculations using VASP. The closest F(HUM)···H($CH_4$) distances are also shown. Atom colors: C = gray, H = white, N = blue, F = cyan, Ti = silver, Cu = gold.

(A) (B)

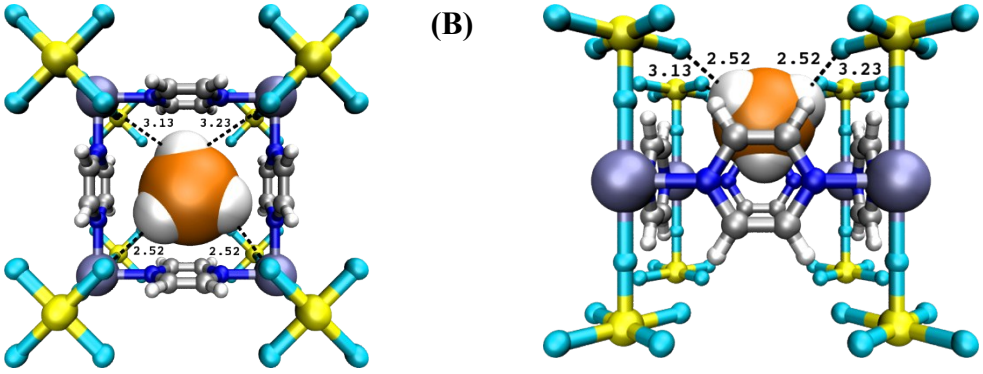


**Supplementary Figure 21.**
Molecular modelleling of $CH_4$ binding site in SIFSIX-3-Ni. (**A**) *c*-axis view (**B**) and a/b-axis view of a portion of the crystal structure of SIFSIX-3-Ni showing the optimized position of a $CH_4$ molecule in the HUM as determine through periodic DFT calculations using VASP. The closest F(HUM)···H($CH_4$) distances are also shown. Atom colors: C = gray, H = white, N = blue, F = cyan, Si = yellow, Ni = lavender.

(A) (B)

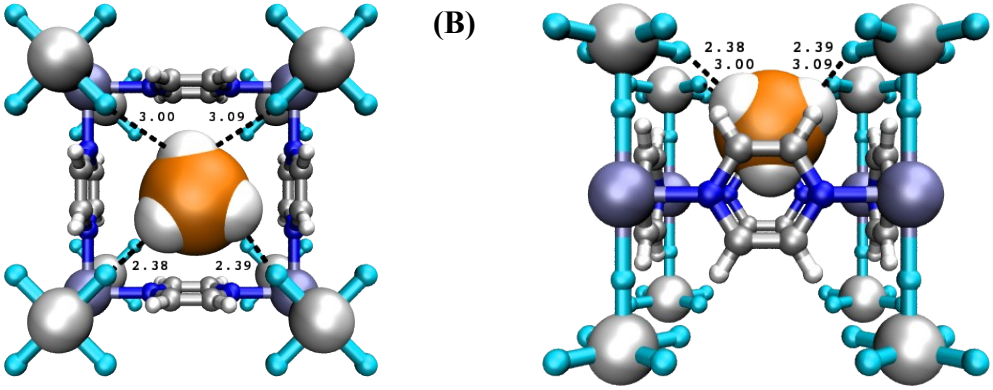


**Supplementary Figure 22.**
Molecular modelling of $CH_4$ binding site in TIFSIX-3-Ni. (**A**) *c*-axis view (**B**) and *a*/*b*-axis view of a portion of the crystal structure of TIFSIX-3-Ni showing the optimized position of a $CH_4$ molecule in the HUM as determine through periodic DFT calculations using VASP. The closest F(HUM)···H($CH_4$) distances are also shown. Atom colors: C = gray, H = white, N = blue, F = cyan, Ti = silver, Ni = lavender.

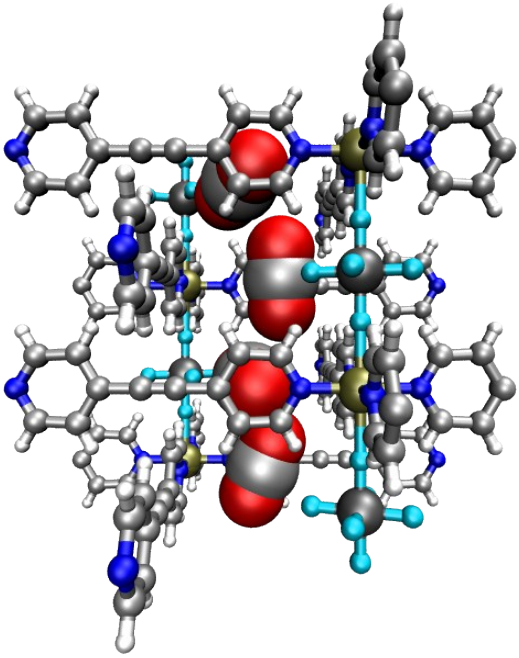

**Supplementary Figure 23.**
Modeled structure of $CO_2$ within a channel of TIFSIX-2-Cu-i. Atom colors: C = cyan, H = white, N = blue, O = red, F = cyan, Ti = silver, Cu = gold (*4, 18*).

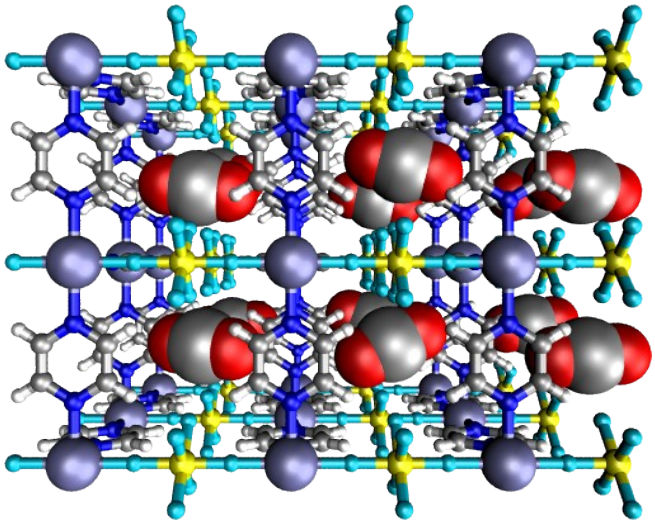

**Supplementary Figure 24.**
Modeled structure of $CO_2$ within the 3 × 3 × 3 system cell of SIFSIX-3-Ni. Note, the terminal pyrazine atoms were removed for clarity. Atom colors: C = cyan, H = white, N = blue, O = red, F = cyan, Si = yellow, Ni = lavender (*4, 18*).

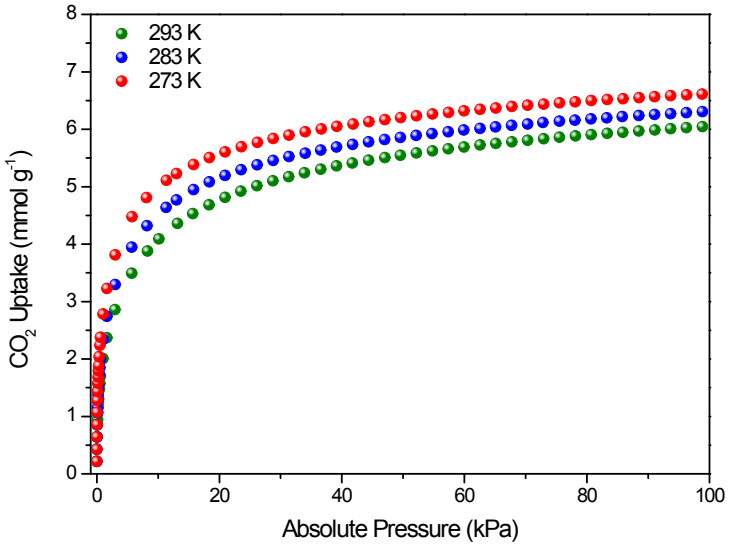


**Supplementary Figure 25.**
Sorption isotherms for $CO_2$ at 273 K, 283 K and 293 K for Zeolite 13X.

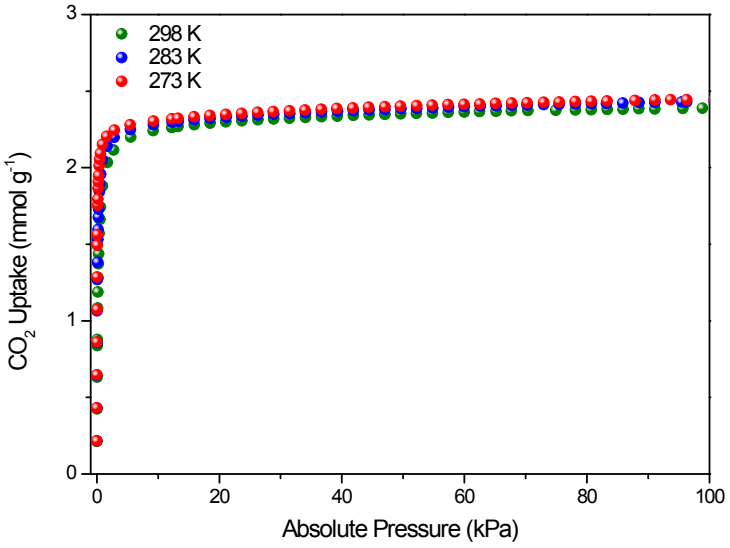


**Supplementary Figure 26.**
Sorption isotherms for $CO_2$ at 273 K, 283 K and 298 K for SIFSIX-3-Ni.

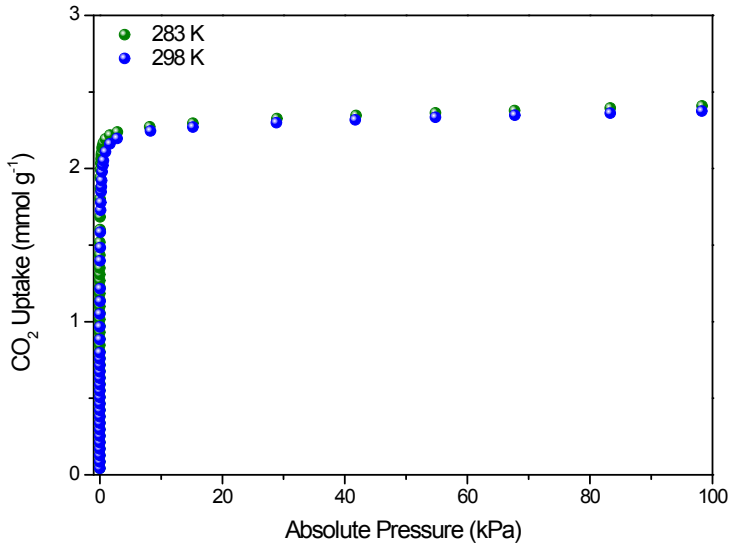


**Supplementary Figure 27.**
Sorption isotherms for $CO_2$ at 283 K and 298 K for TIFSIX-3-Ni.

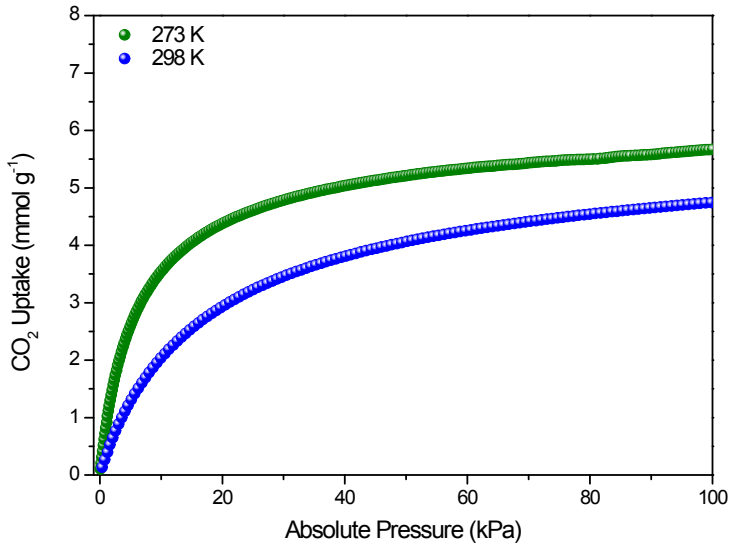


**Supplementary Figure 28.**
Sorption isotherms for $CO_2$ at 273 K and 298 K for TIFSIX-2-Cu-i.

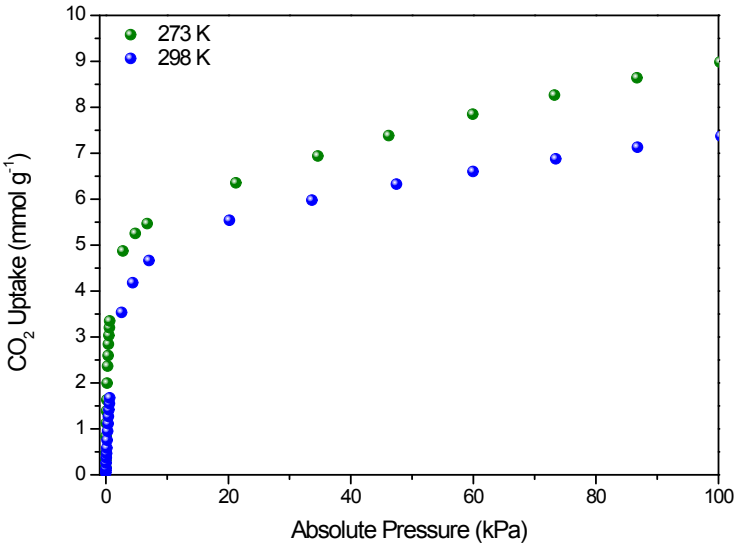


**Supplementary Figure 29.**
Sorption isotherms for $CO_2$ at 273 K and 298 K for Mg-MOF-74.

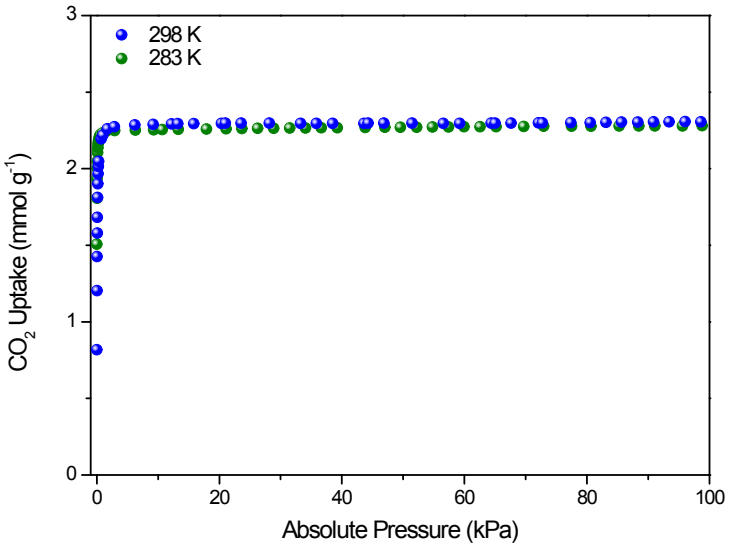


**Supplementary Figure 30.**
Sorption isotherms for $CO_2$ at 283 K and 298 K for NbOFFIVE-1-Ni.

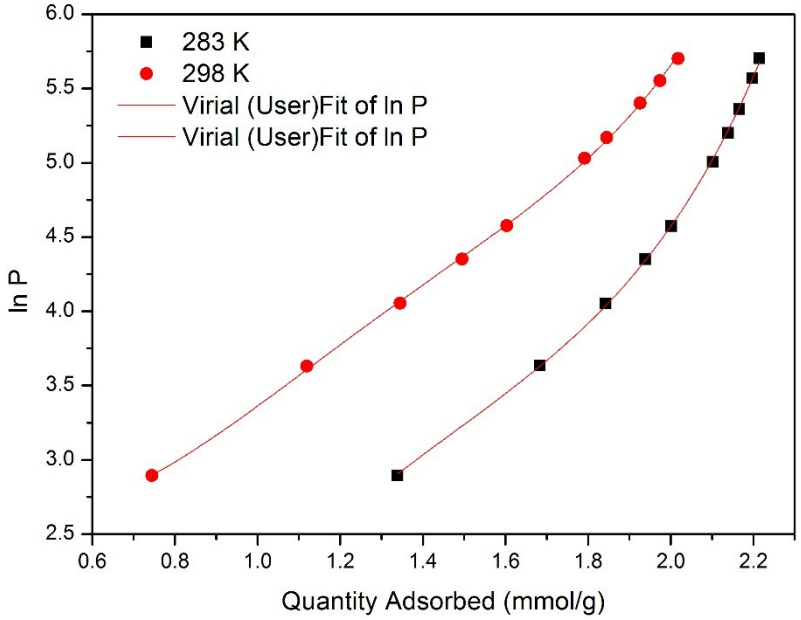


**Supplementary Figure 31.**
Fitting of the isotherm data of TIFSIX-3-Ni to the virial equation.

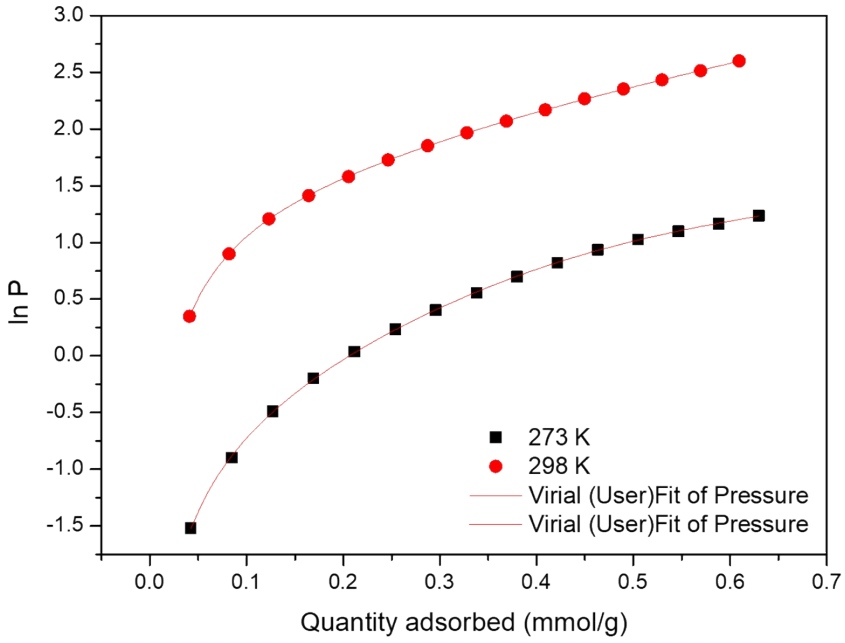


**Supplementary Figure 32.**
Fitting of the isotherm data of NbOFFIVE-1-Ni to the virial equation.

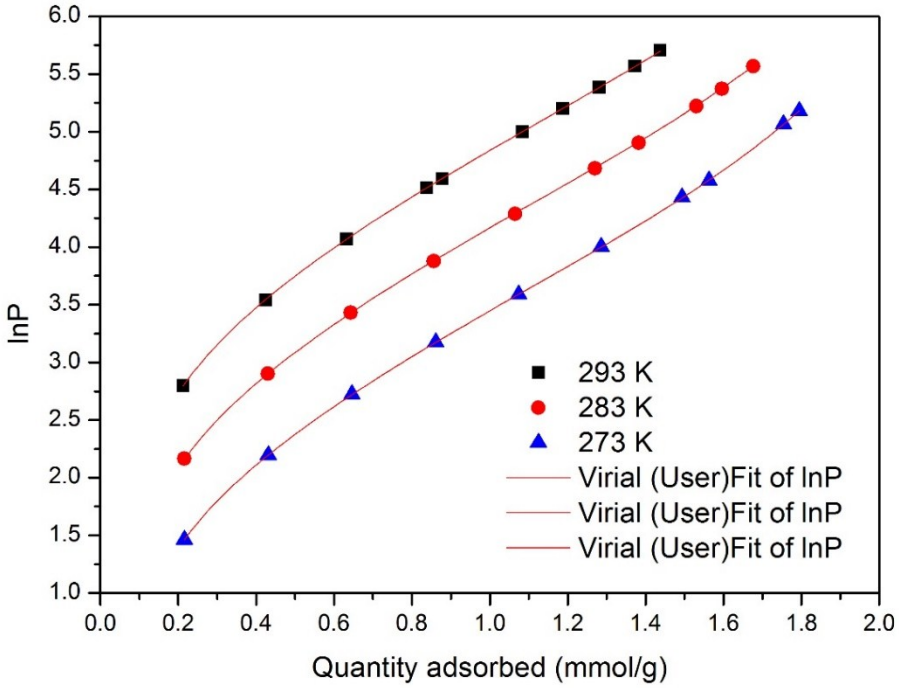


**Supplementary Figure 33.**
Fitting of the isotherm data of SIFSIX-3-Ni to the virial equation.

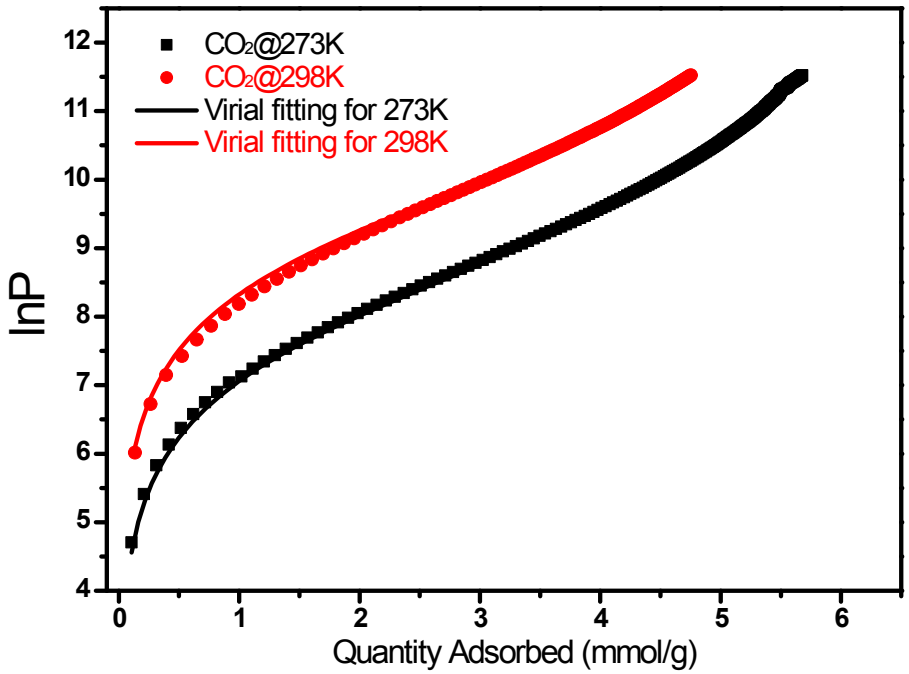


**Supplementary Figure 34.**
Fitting of the isotherm data of TIFSIX-2-Cu-i to the virial equation.

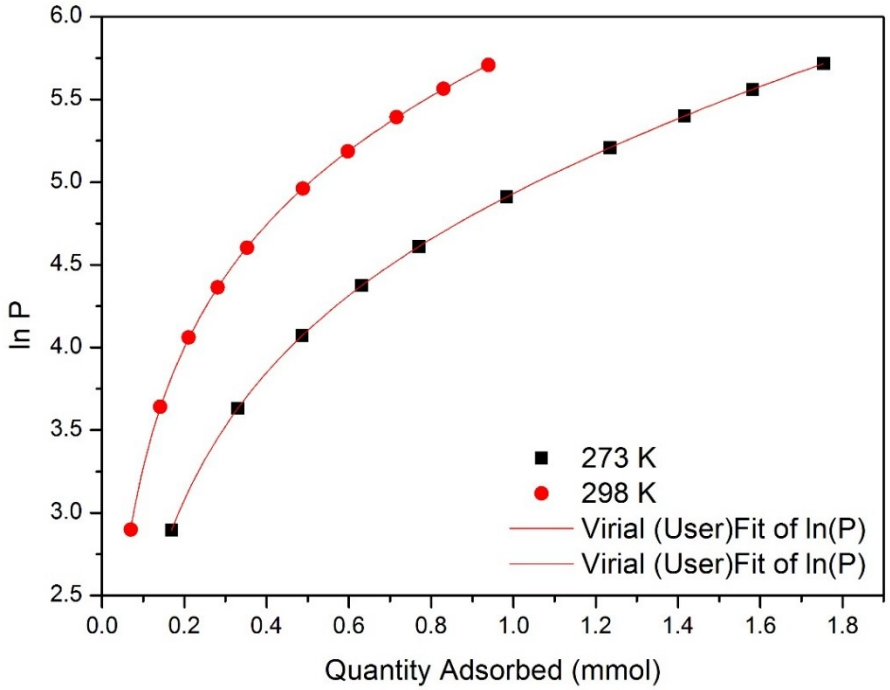


**Supplementary Figure 35.**
Fitting of the isotherm data of Mg-MOF-74 to the virial equation.

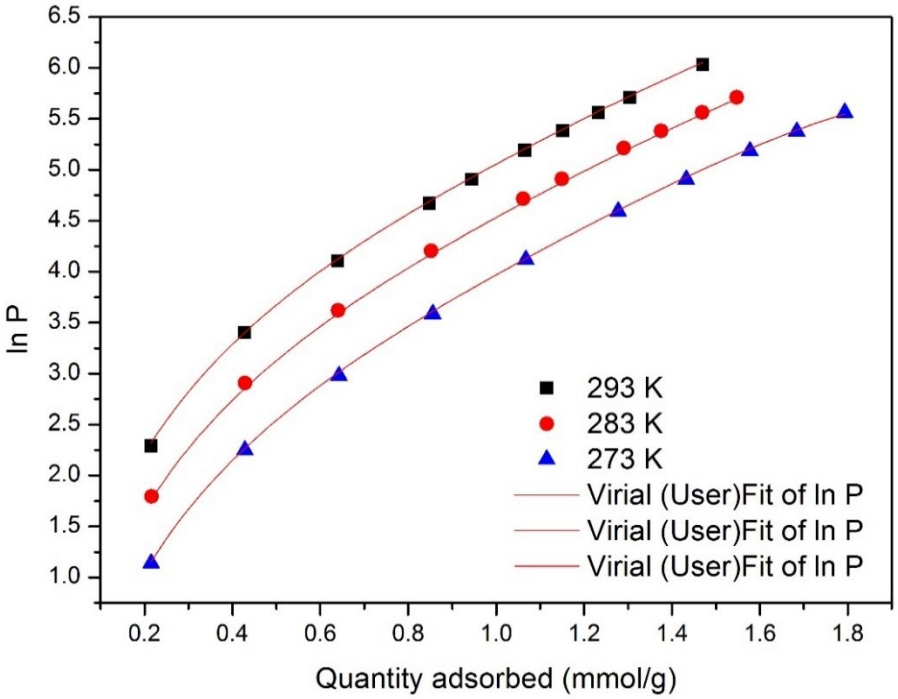


**Supplementary Figure 36.**
Fitting of the isotherm data of Zeolite 13X to the virial equation.

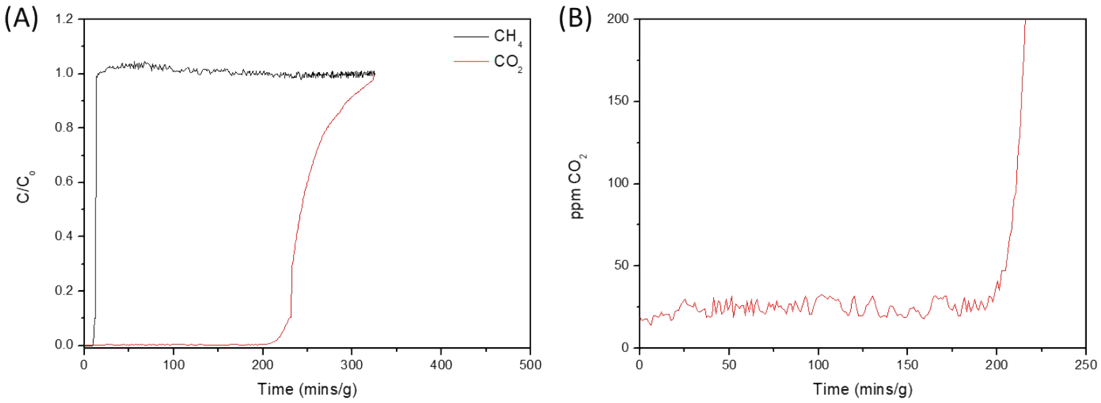


**Supplementary Figure 37.**
Dynamic breakthrough curves. (A) 1% $CO_2$/99% $CH_4$ breakthrough performance and (B) effluent $CO_2$ concentration for TIFSIX-3-Ni at 298K, 20 ml/min flow.

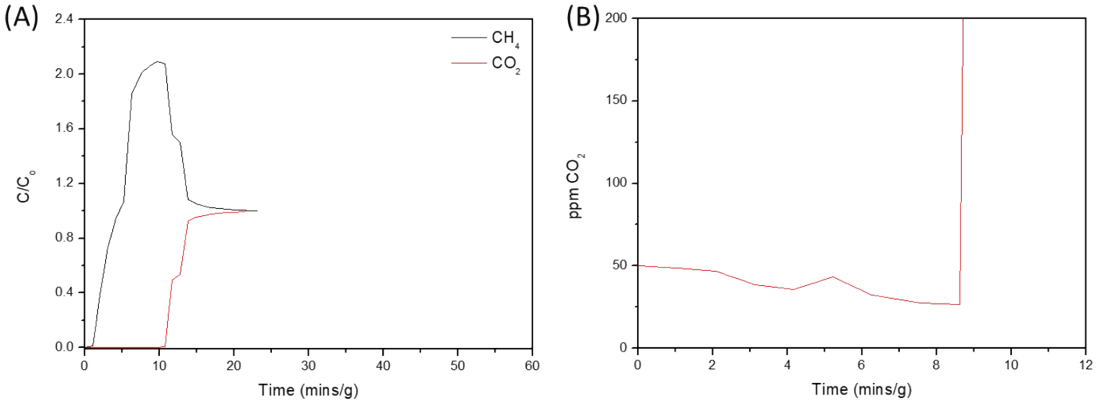


**Supplementary Figure 38.**
Dynamic breakthrough curves. (A) 50% $CO_2$/50% $CH_4$ breakthrough performance and (B) effluent $CO_2$ concentration for TIFSIX-3-Ni at 298K, 10 ml/min flow.

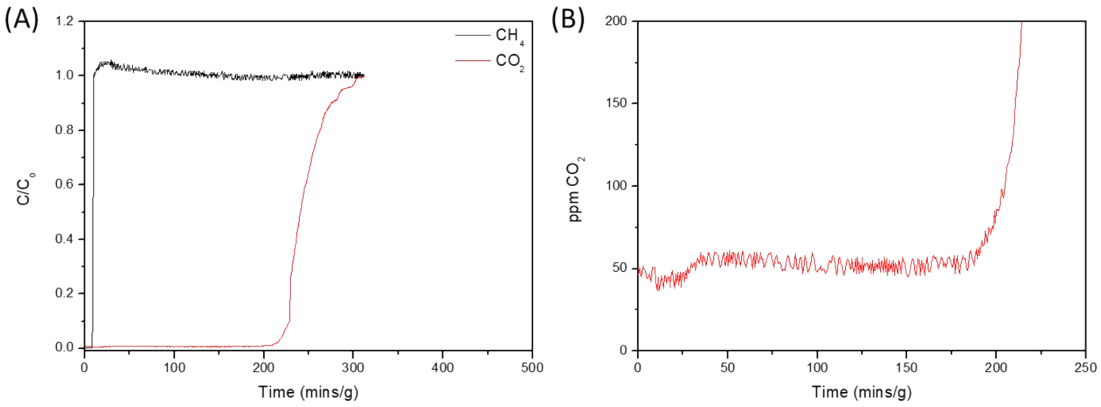


**Supplementary Figure 39.**
Dynamic breakthrough curves. (A) 1% $CO_2$/99% $CH_4$ breakthrough performance and (B) effluent $CO_2$ concentration for NbOFFIVE-1-Ni at 298K, 20 ml/min flow.

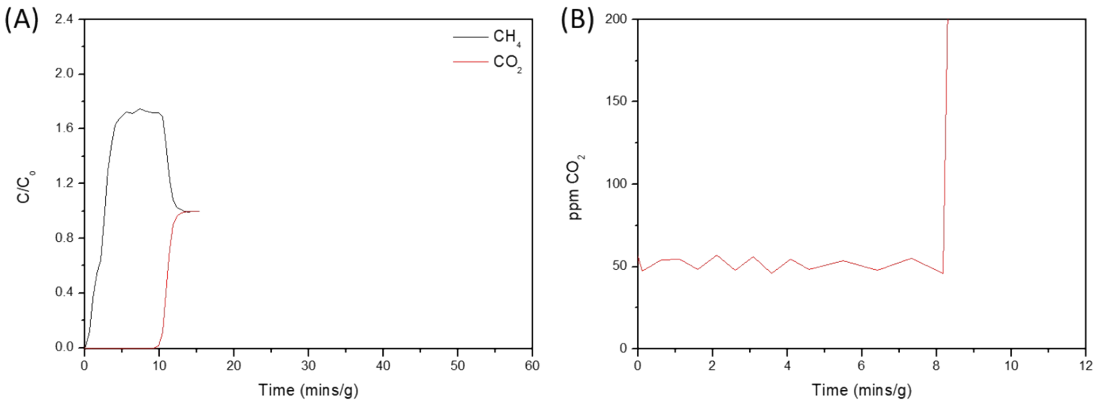


**Supplementary Figure 40.**
Dynamic breakthrough curves. (A) 50% $CO_2$/50% $CH_4$ breakthrough performance and (B) effluent $CO_2$ concentration for NbOFFIVE-1-Ni at 298K, 10 ml/min flow.

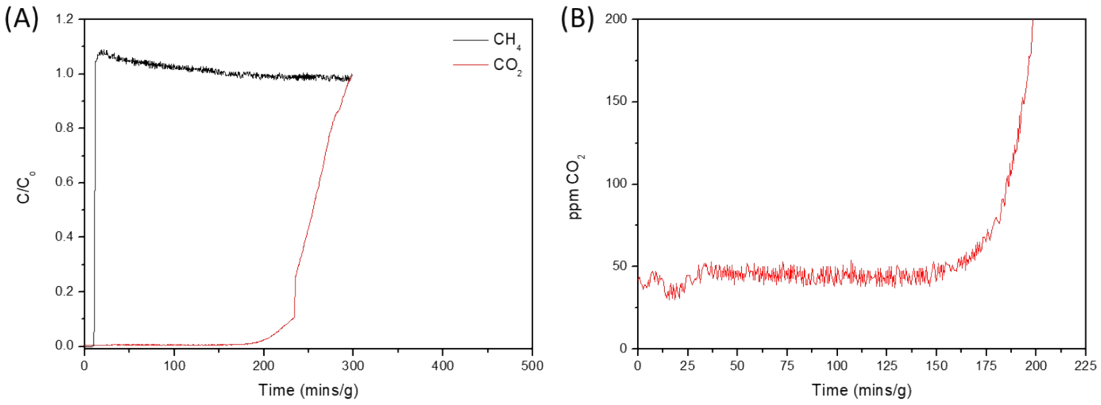


**Supplementary Figure 41.**
Dynamic breakthrough curves. (A) 1% $CO_2$/99% $CH_4$ breakthrough performance and (B) effluent $CO_2$ concentration for SIFSIX-3-Ni at 298K, 20 ml/min flow.

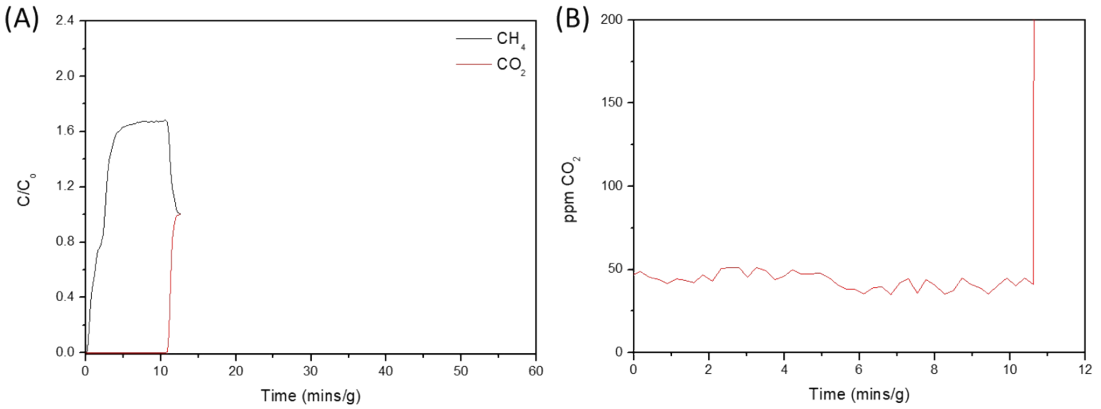


**Supplementary Figure 42.**
Dynamic breakthrough curves. (A) 50% $CO_2$/50% $CH_4$ breakthrough performance and (B) effluent $CO_2$ concentration for SIFSIX-3-Ni at 298K, 10 ml/min flow.

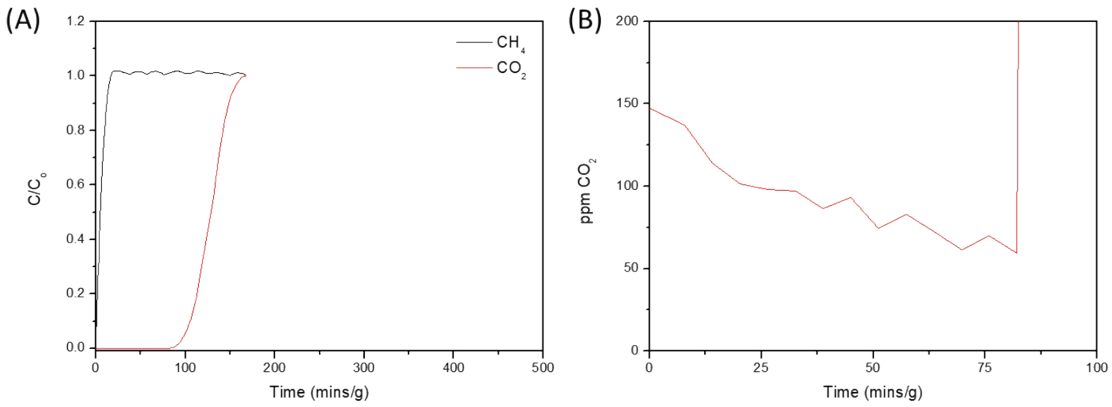


**Supplementary Figure 43.**
Dynamic breakthrough curves. (A) 1% $CO_2$/99% $CH_4$ breakthrough performance and (B) effluent $CO_2$ concentration for TIFSIX-2-Cu-i at 298K, 20 ml/min flow.

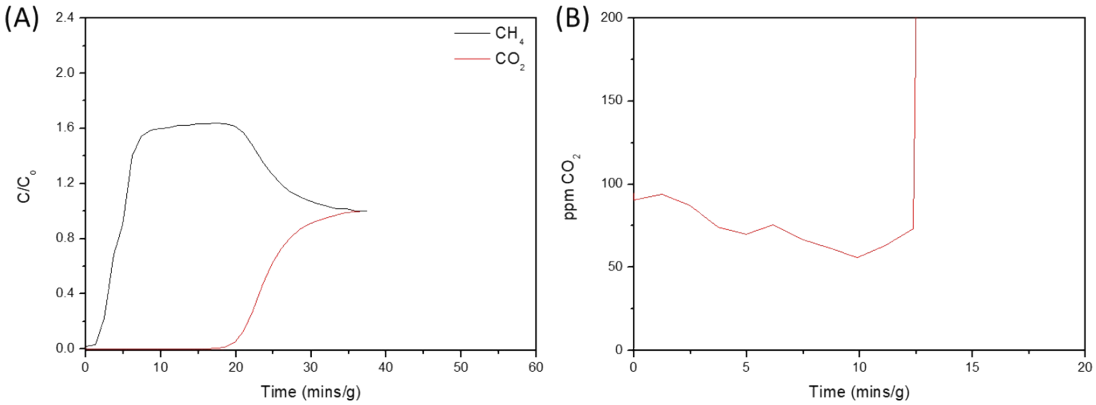


**Supplementary Figure 44.**
Dynamic breakthrough curves. (A) 50% $CO_2$/50% $CH_4$ breakthrough performance and (B) effluent $CO_2$ concentration for TIFSIX-2-Cu-i at 298K, 10 ml/min flow.

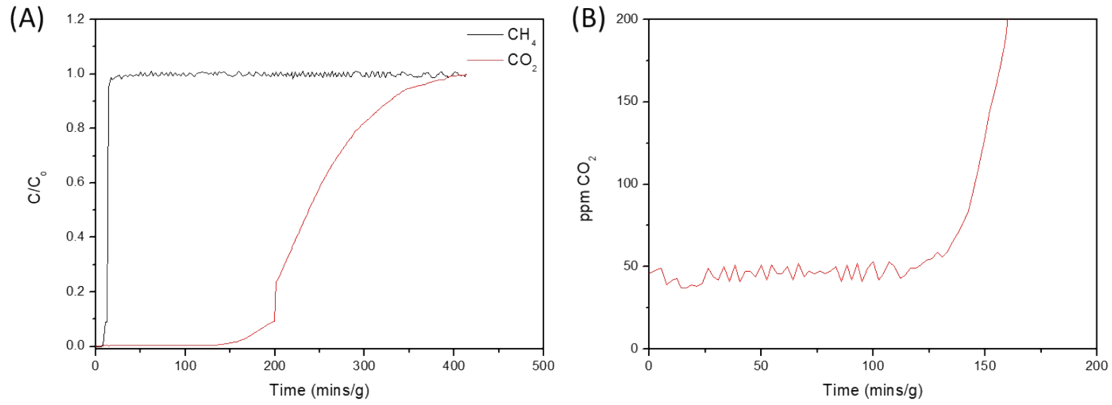


**Supplementary Figure 45.**
Dynamic breakthrough curves. (A) 1% $CO_2$/99% $CH_4$ breakthrough performance and (B) effluent $CO_2$ concentration for Mg-MOF-74 at 298K, 20 ml/min flow.

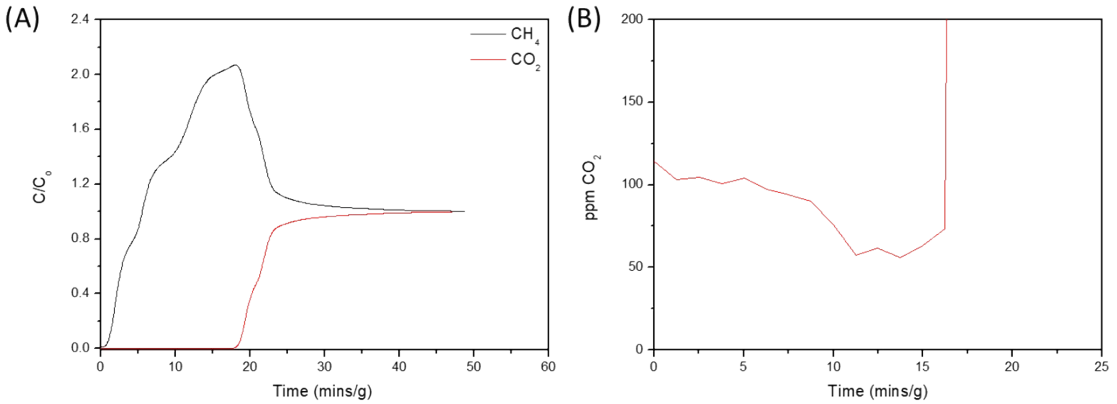


**Supplementary Figure 46.**
Dynamic breakthrough curves. (A) 50% $CO_2$/50% $CH_4$ breakthrough performance and (B) effluent $CO_2$ concentration for Mg-MOF-74 at 298K, 10 ml/min flow.

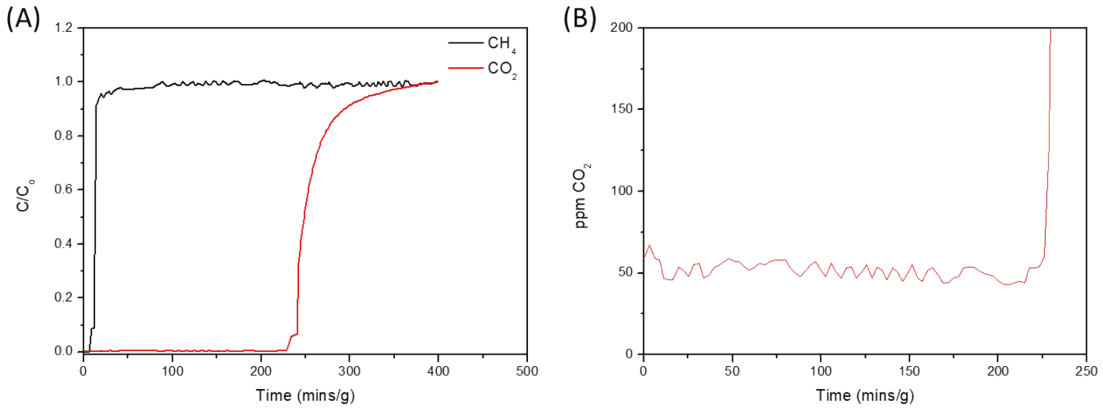


**Supplementary Figure 47.**
Dynamic breakthrough curves. (A) 1% $CO_2$/99% $CH_4$ breakthrough performance and (B) effluent $CO_2$ concentration for Zeolite 13X at 298K, 20 ml/min flow.

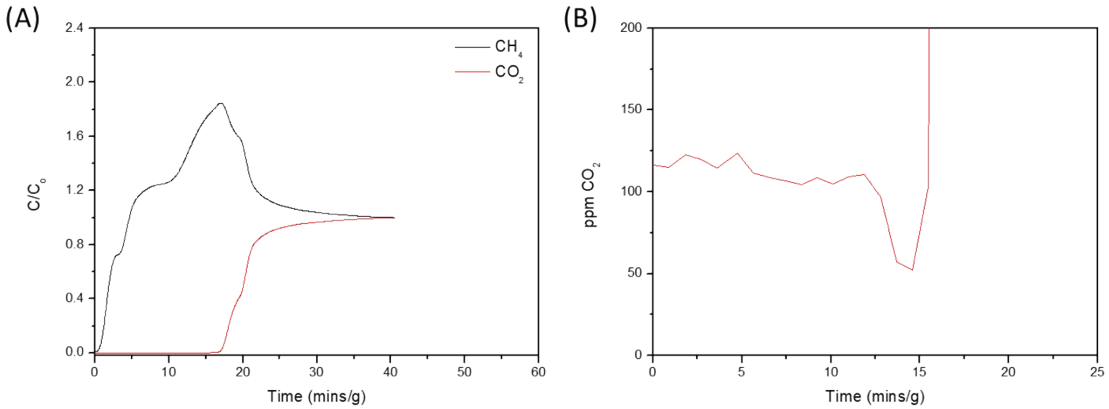


**Supplementary Figure 48.**
Dynamic breakthrough curves. (A) 50% $CO_2$/50% $CH_4$ breakthrough performance and (B) effluent $CO_2$ concentration for Zeolite 13X at 298K, 10 ml/min flow.

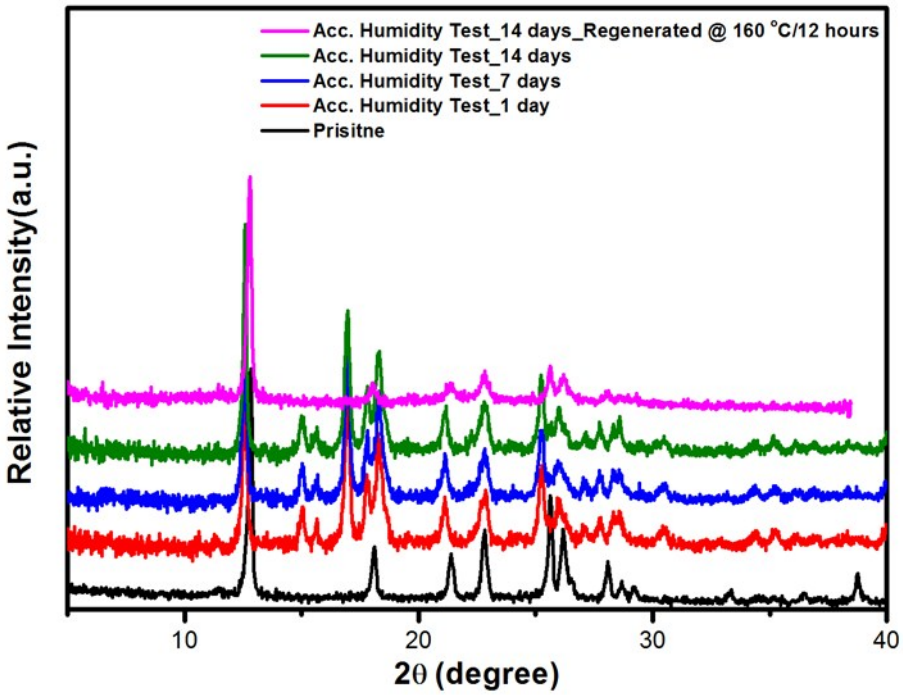


**Supplementary Figure 49.**
Powder X-ray diffraction (PXRD) for TIFSIX-3-Ni after 1, 7 and 14 days accelerated stability testing.

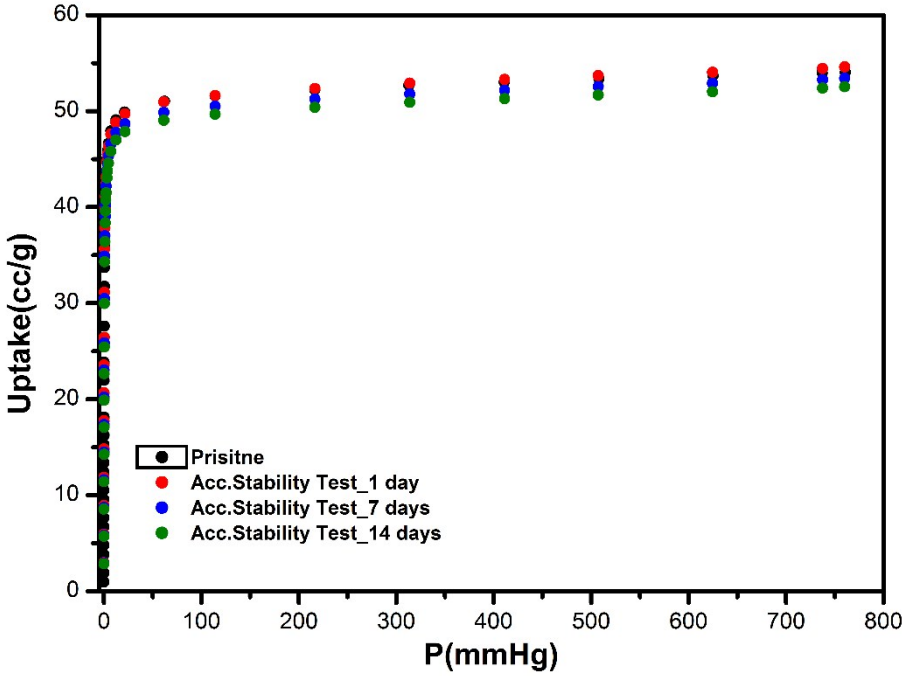


**Supplementary Figure 50.**
$CO_2$ sorption for TIFSIX-3-Ni after 1, 7 and 14 days accelerated stability testing.

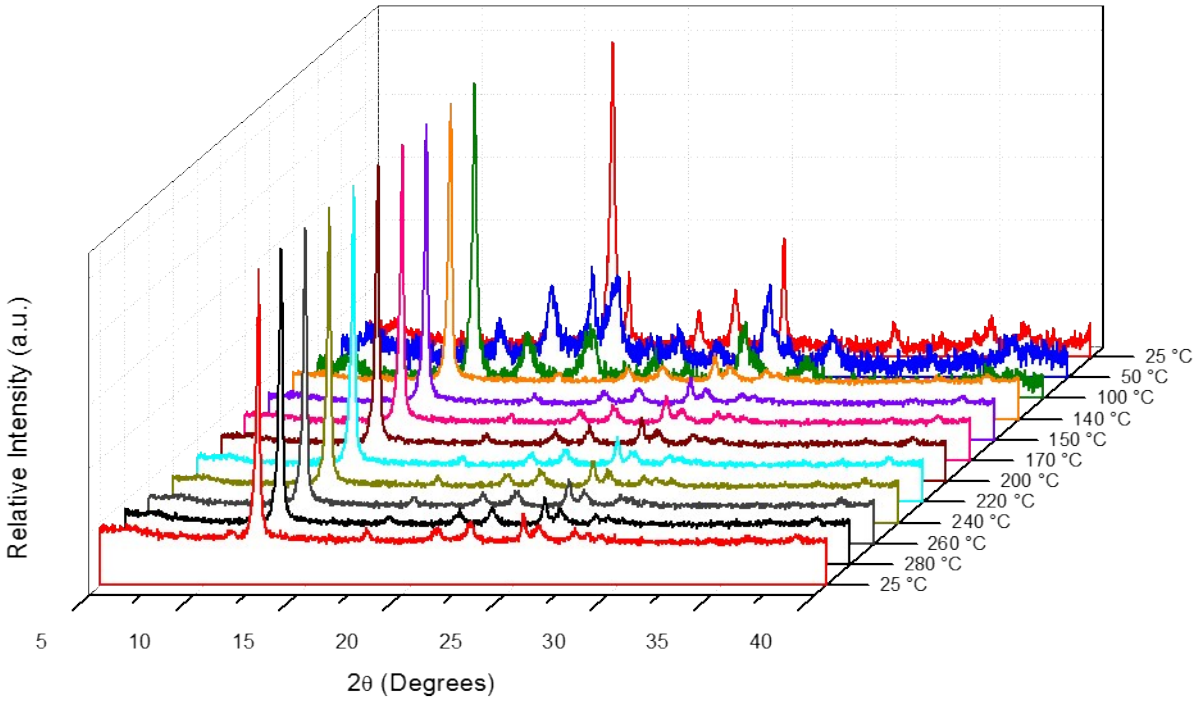


**Supplementary Figure 51.**
Variable temperature powder X-ray diffraction (VT-PXRD) for TIFSIX-3-Ni.

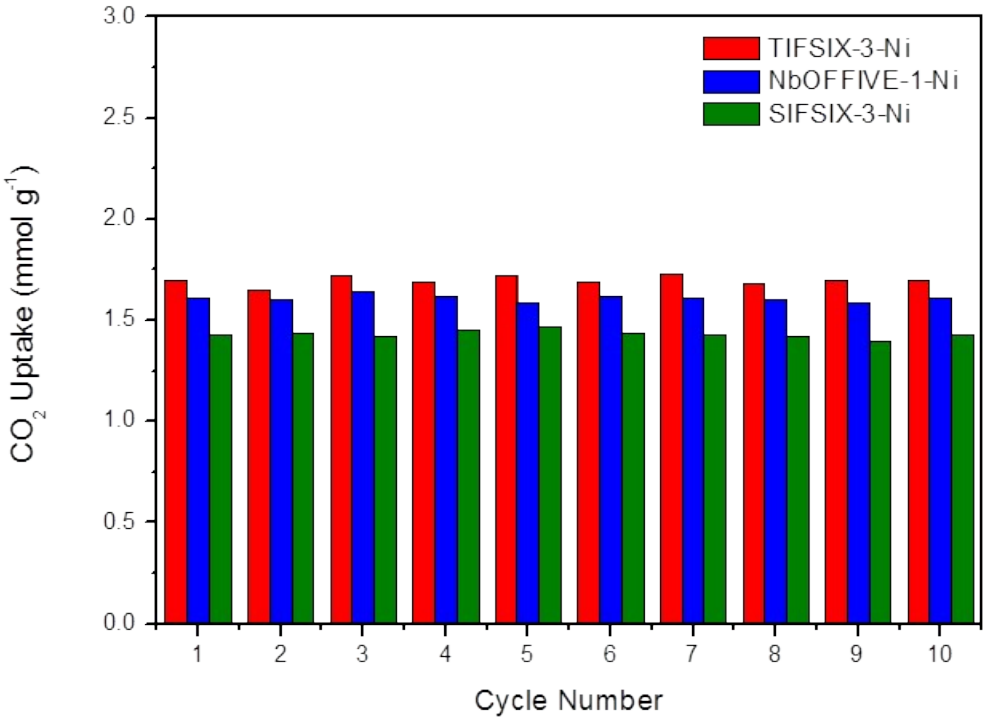


**Supplementary Figure 52.**
Cyclability of HUMs in 1% $CO_2$/99% $CH_4$ Breakthrough Studies, regeneration at 80 °C.

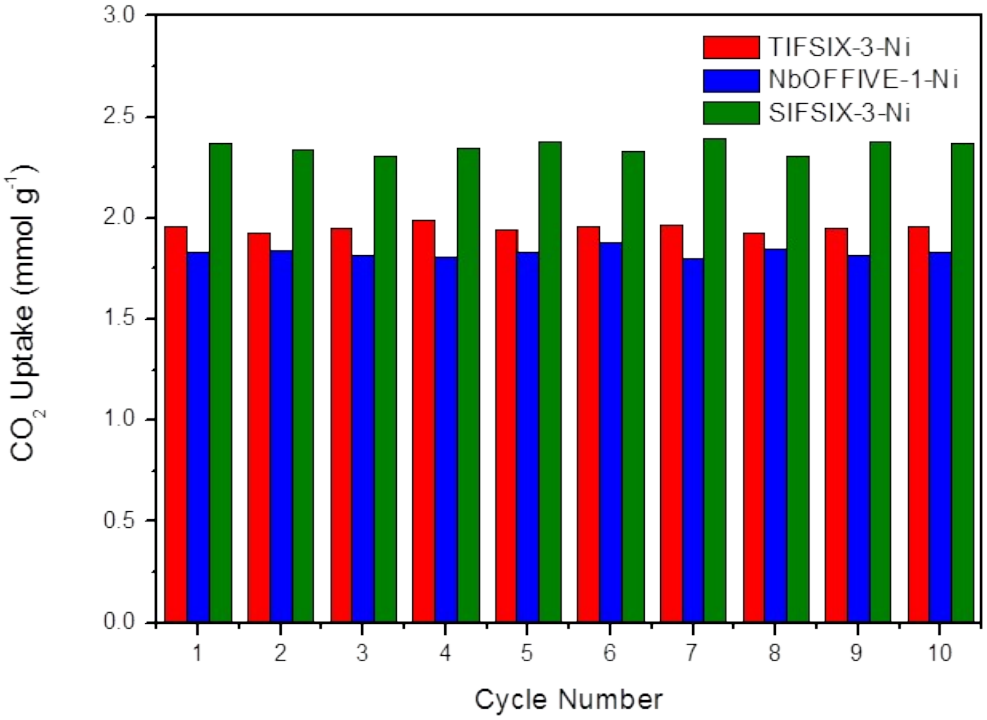


**Supplementary Figure 53.**
Cyclability of HUMs in 50% $CO_2$/50% $CH_4$ Breakthrough Studies, regeneration at 80 °C.

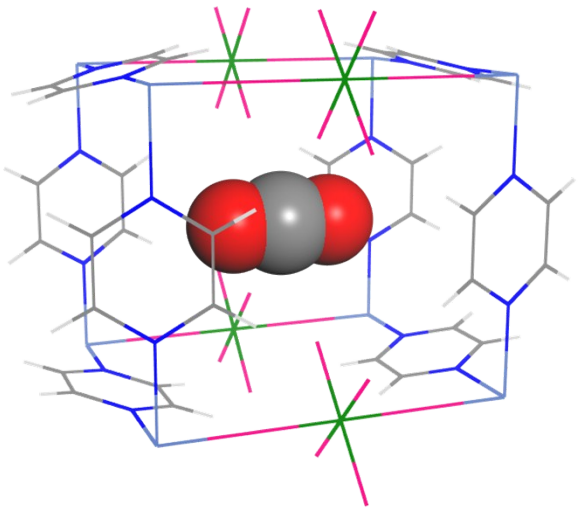

**Supplementary Figure 54.**
$CO_2$ loaded structure for TIFSIX-3-Ni ($CO_2$@TIFSIX-3-Ni) as determined from in situ synchrotron powder X-ray diffractions (PXRD) *(1)*.

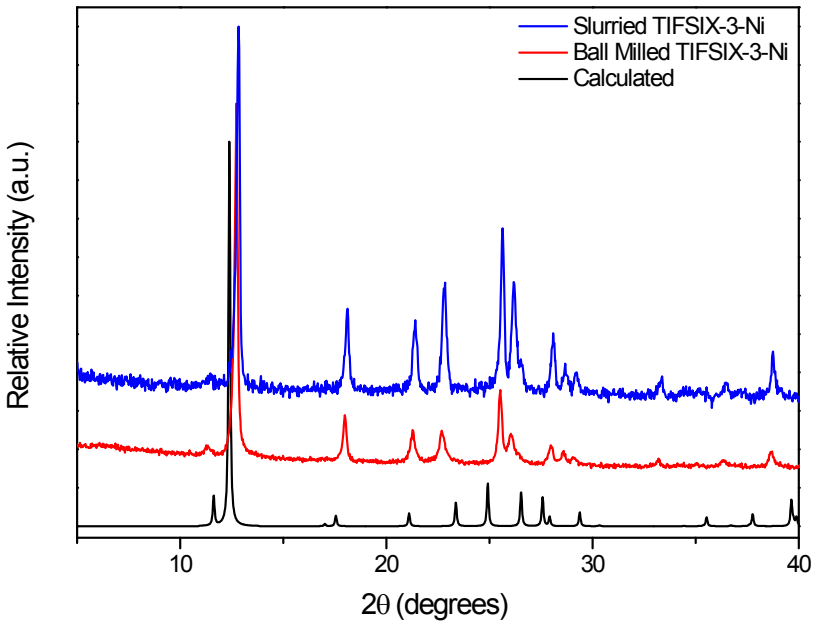


**Supplementary Figure 55.**
Powder X-ray diffraction (PXRD) for TIFSIX-3-Ni prepared *via* mechanochemical ball milling and slurrying methods.

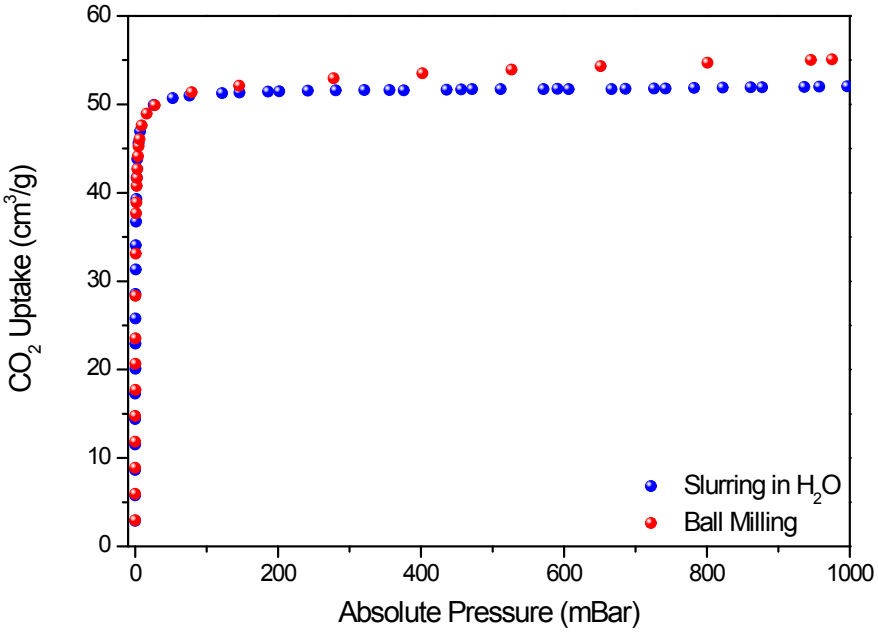


**Supplementary Figure 56.**
$CO_2$ gas sorption uptake at 25 °C for TIFSIX-3-Ni prepared *via* mechanochemical ball milling and slurrying methods.

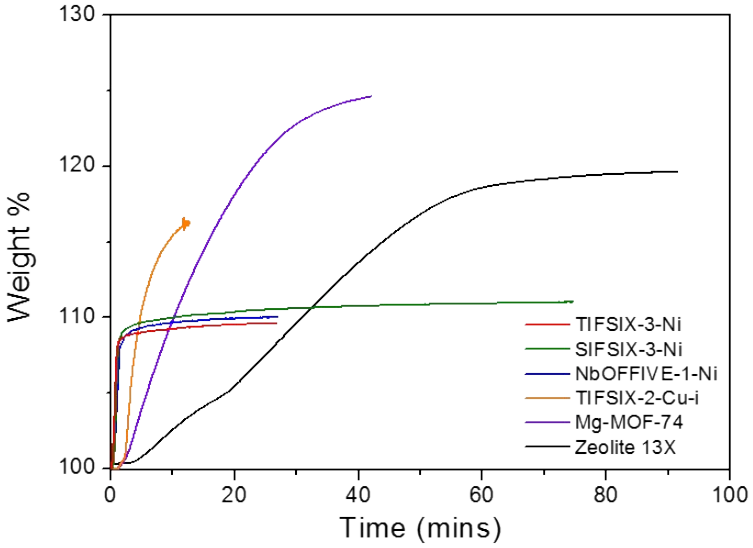


**Supplementary Figure 57.**
1.0 bar gravimetric $CO_2$ uptake versus time for six physisorbents studied at 298 K.

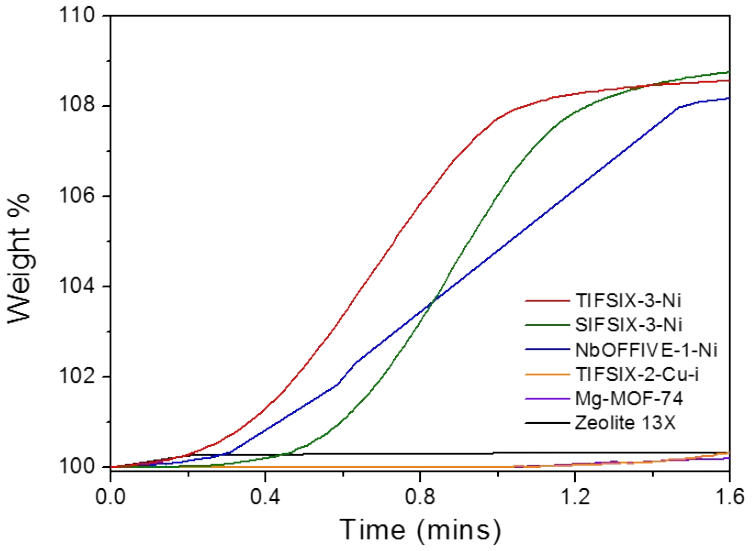


**Supplementary Figure 58.**
$CO_2$ uptake kinetics for TIFSIX-3-Ni, SIFSIX-3-Ni and NbOFFIVE-1-Ni at 1.0 bar $CO_2$ and 308 K.

## References


1. A. Kumar *et al.*, Hybrid ultramicroporous materials (HUMs) with enhanced stability and trace carbon capture performance. *Chem. Commun.,* **53**, 5946-5949 (2017).
2. A. Cadiau, K. Adil, P. Bhatt, Y. Belmabkhout, M. Eddaoudi, A metal-organic framework–based splitter for separating propylene from propane. *Science,* **353**, 137-140 (2016).
3. S. K. Elsaidi *et al.*, Hydrophobic pillared square grids for selective removal of $CO_2$ from simulated flue gas. *Chem. Commun.,* **51**, 15530-15533 (2015).
4. K.-J. Chen *et al.*, Benchmark $C_2H_2/CO_2$ and $CO_2/C_2H_2$ separation by two closely related hybrid ultramicroporous materials. *CHEM* **1**, 753-765 (2016).
5. S. R. Caskey, A. G. Wong-Foy, A. J. Matzger, Dramatic tuning of carbon dioxide uptake via metal substitution in a coordination polymer with cylindrical pores. *J. Am. Chem. Soc.,* **130**, 10870-10871 (2008).
6. A. Kumar *et al.*, Direct air capture of $CO_2$ by physisorbent materials. *Angew. Chem. Int. Ed.,* **54**, 14372-14377 (2015).
7. J. A. Mason *et al.*, Application of a high-throughput analyzer in evaluating solid adsorbents for post-combustion carbon capture via multicomponent adsorption of $CO_2$, $N_2$, and $H_2O$. *J. Am. Chem. Soc.,* **137**, 4787-4803 (2015).
8. A. L. Myers, J. M. Prausnitz, Thermodynamics of mixed-gas adsorption. *AIChE J.,* **11**, 121-127 (1965).
9. G. Kresse, J. Hafner, Ab initio molecular-dynamics simulation of the liquid-metal-amorphous-semiconductor transition in germanium. *Phys. Rev. B Condens. Matter.,* **49**, 14251-14269 (1994).
10. G. Kresse, J. Hafner, Ab initio molecular dynamics for liquid metals. *Phys. Rev. B Condens. Matter.,* **47**, 558-561 (1993).
11. G. Kresse, J. Furthmüller, Efficiency of ab-initio total energy calculations for metals and semiconductors using a plane-wave basis set. *Comput. Mater. Sci.,* **6**, 15-50 (1996).
12. G. Kresse, J. Furthmüller, Efficient iterative schemes for ab initio total-energy calculations using a plane-wave basis set. *Phys. Rev. B Condens. Matter.,* **54**, 11169 (1996).
13. P. E. Blochl, Projector augmented-wave method. *Phys. Rev. B Condens. Matter.,* **50**, 17953-17979 (1994).
14. G. Kresse, D. Joubert, From ultrasoft pseudopotentials to the projector augmented-wave method. *Phys. Rev. B Condens. Matter.,* **59**, 1758 (1999).
15. J. P. Perdew, K. Burke, M. Ernzerhof, Generalized gradient approximation made simple. *Phys. Rev. Lett.,* **77**, 3865 (1996).
16. J. P. Perdew, K. Burke, M. Ernzerhof, Generalized gradient approximation made simple [Phys. Rev. Lett. 77, 3865 (1996)]. *Phys. Rev. Lett.,* **78**, 1396 (1997).
17. S. Grimme, Semiempirical GGA-type density functional constructed with a long-range dispersion correction. *J. Comput. Chem.,* **27**, 1787-1799 (2006).
18. P. Nugent *et al.*, Porous materials with optimal adsorption thermodynamics and kinetics for $CO_2$ separation. *Nature,* **495**, 80-84 (2013).